UNIVERSITY OF TEXAS AT ARLINGTON

Synthesis of nickel-titanium intermetallic surface coatings via electroylytic plasma processing

by

Brody Allen Moore

Presented to the Faculty of the Graduate School of Materials Science and Engineering
The University of Texas at Arlington in Partial Fulfillment
of the requirements
for the MS Degree

MASTER OF SCIENCE

Advisor:
Dr. Efstathios "Stathis" I. Meletis
Department of Materials Science and Engineering
THE UNIVERSITY OF TEXAS AT ARLINGTON

May 2020

"...rise above, focus on science."

Rick Sanchez

UNIVERSITY OF TEXAS AT ARLINGTON

Abstract

Dr. Efstathios "Stathis" I. Meletis

Department of Materials Science and Engineering

Master of Science

by Brody Allen Moore

Electrolytic plasma processing (EPP) is an environmentally friendly surface cleaning and deposition technique. Dependant on circuit polarity, anionic or cationic species can be deposited from an aqueous electrolyte bridge, resulting in characteristic nanograin surface morphology and very high deposition rates. This work was conducted to study the EPP process, develop optimal parameters for the synthesis of very hard surface coatings, and study the resultant physical and electrochemical properties of produced titanium-nickel intermetallic surfaces.

This study focuses on Ni deposited onto pure Ti surfaces for improvement of surface wear, hardness, and corrosion properties while retaining uncompromised Ti bulk characteristics. The surface of the coatings as well as properties of the interface are studied in order to understand resultant Nickel surface film characteristics as well as the intermetallic formation within the interface. Microstructure, morphology, wear and corrosion properties, and phases are studied via electron microscopy, profilometry, x-ray diffraction, anodic polarization, and wear testing. The EPP cleaning of Ti is briefly outlined and supported by literature and findings of fellow UTA Surface and Nanoengineering Laboratory (SaNEL) researchers.

Acknowledgements

I would like to acknowledge and thank my family for their endless support.

I would like to acknowledge and thank Dr. Meletis for having me in the SaNEL research group and for giving me the opportunity to conduct this research.

I woud like to acknowledge and thank Dr. Jiang for assisting and training me in my thesis analysis.

I would like to acknowledge and thank the other SaNEL researchers for their support and assistance.

Contents

List of Figures

List of Tables

Chapter 1

Introduction

1.1 Motivation

Titanium is valuable in medical, construction and aviation industries due to its high strength, comparable to steel alloys, and very low density. However, pure titanium loses value in applications where surface wear and corrosion become dominant factors Miller and Holladay [1958]. As a result, the application of surface modifying coatings boasting high hardness and high wear resistance would be of great importance to industries utilizing titanium in a wear-prone system. In such systems, titanium alloys have gained recognition as high performance wear resistant and corrosion resistant solutions Rominiyi et al. [2020]. Titanium-nickel alloys display interesting properties dependant on nickel content. For example, the stoichiometric compound is a shape-memory alloy, proposed for use in microcontrollers, while the high titanium alloys are very hard and wear resistant.

Much work has been done on improving the surface of titanium through coatings, oxidizing, nitriding, etc Muraleedharan and Meletis [1992]. It has long been apparent that the

titanium surface can be dramatically improved by lubricating a titanium oxide layer to inhibit fretting and wear. Additionally, coating titanium with more advanced metallic processes have been studied. For example, Titanium-Nickel-Nitride coatings are used to inhibit corrosion in orhtodontic arc wires while keeping the shape-memory properties of the bulk uninterrupted Starosvetsky and Gotman [2001].

The motivation for this thesis is to explore the possible formation of Ti-Ni intermetallic coatings via deposition of Ni on Ti surfaces by the EPP process and subsequently characterize the produced coatings. Ti-Ni intermetallics boast very high hardness and have the potential to significantly boost wear resistance, while nickel surfaces tend to outperform titanium surfaces in corrosive work environments, especially in the presence of chloride ions. The EPP deposition technique is used for its ability to cleanly deposit nickel on the surface, as well as the high temperature mixing effect expected of leading to intermetallic layers within the deposited film.

1.2 Research Objectives

The EPP (Electrolytic Plasma Processing) deposition mechanism has recently become a topic of study over the last 15 years. Previous researchers in the UTA SaNEL laboratory have studied the EPP cleaning process, EPP deposition of zinc, nickel, and molybdenum onto an iron substrate Cionea [2010] and EPP deposition of nickel onto an aluminum substrate Smith [2014], as well as oxide building with alumina-zirconia Barati [2018]. While previous studies have studied the formation of intermetallics throughout a coating, most notabley Smith (2014) studying Ni-Al intermetallic coatings, an in depth study has never been conducted with Ti-Ni intermetallics and if they can be formed in the EPP deposition process. As a result of vast amounts of previous knowledge and research, the

EPP cleaning process is studied with Fe and Ti to determine functionality and optimal processing parameters, then the Ni deposition process is undertaken to characterize the produced surface and interface (cross section EDS, TEM, SEM) and subsequently study surface properties of deposited films (hardness, wear resistance, corrosion, morphology).

Chapter 2

Literature Review

2.1 Nickel Coatings

The proposed surface changes in this thesis revolve around deposition of a pure nickel coating. Nickel deposition has been studied extensively and a multitude of valid deposition methods are in use today. Notable depositon methods include laser alloying Song et al. [2019], sputtering Stock et al. [2008], chemical vapor deposition Chandrakala et al. [2017], plasma spraying Liu et al. [2019] and electroless depositon Wei et al..

The most broadly used technology is the electroless coating, in which nickel electroless coatings are far in a way the most popular choice of media due to increased corrosion and wear resistance. The electroless process requires a series of harsh chemical treatments with dangerous acids and bases in order to prepare the substrate for electroless plating. Foregoing the full range of chemical treatments inhibits adhesion of the electroless coating due to oxide development before the film can bond. This problem is most noticeable in titanium and aluminum, both of which form strong oxides very quickly Sahoo and

Das [2011]. The electroless deposition follows a series of acid bathing steps for surface cleaning and oxide removal, as follows Umapathi et al. [2020]:

1. Ultrasonic Cleaning
2. DI water rinse
3. NaOH Acid bath
4. HCl Acid bath
5. DI water rinse
6. HNO_3 Acid bath
7. NaOH Acid Bath

The electroless plating process does not require external power, unlike electroplating techniques, instead relying on several chemical reaction steps to form compounds with great adhesion. With a clean surface, the substrate is treated with a Pd^{2+} activation method and the surface is submerged in a ion rich solution for self assembly. For Ni plating, a Ni_{2+} rich solution like $NiSO_4$ is the selected media. The activated substrate undergoes chemical formation of a double-layer composite coating defined by the operating conditions (Temperature, pH, Stirring speed) and the bath composition Shang et al. [2019].

Other studies of Ni coating technology have shown great increase in surface properties regardless of deposition technique. Ni coatings on Nb-TiAl alloys created by plasma surface alloying showed great adhesion and increase microhardness via Vicker's hardness testing over uncoated substrates with further hardness increase at higher processing temperature Wang et al. [2020]. Additionally, studies done by the Surface and Nanoengineering

Laboratory (SaNEL) of UTA have produced Ni coatings via EPP, Electroplating, and DC Sputtering Smith [2014], Guidry et al. [2009] showing similar improvements across all surface properties.

2.2 Intermetallic Coatings

There exist several stable intermetallic compounds consisting of nickel titanates including NiTi, Ti_2Ni, Ti_2Ni_3 and Ni_3Ti Adharapurapu [2007]. While the focus of this study lies in synthesis of these very hard shape-memory alloys, no studies have been conducted on them in the EPP/PEO realm. However, prior research done on cold spraying and post treatment processes involving Ni-Ti intermetallics have shown great promise. Cold spraying is a technique in which powders of the selected deposition media are mixed into a solution to be driven through a high pressure nozzle at short distance and appropriate processing temperatures (on the order of 500°C). In order to insure good adhesion and integration of sprayed particles, argon protected annealing processes are carried out at higher temperatures up to 1000°C and then furnace cooled. Researchers found that Ni-Ti intermetallic coatings created in this fashion benefit greatly from post process annealing and friction mixing, increasing porosity via the Kirkendall Effect, mechanical properties (microhardness, wear resistance, density, etc.) and microstructure Huang et al. [2018]. Samples produced by Huang et al. boasted a 4.5 fold increase of microhardness properties after annealing and friction stiring.

EPP/PEO studies carried out by Smith [2014] and Barati [2018] showed that coatings produced by the EPP/PEO process display good coverage given appropriate deposition time, rapid growth rate, and increases in corrosion resistance over the underlying

substrate when intermetallics are being produced (Ni-Al in the case of Smith, Alumina-Zirconia in the case of Barati) Smith [2014], Barati [2018].

2.2.1 Theoretical Hardness Data for Ni-Ti Intermetallics

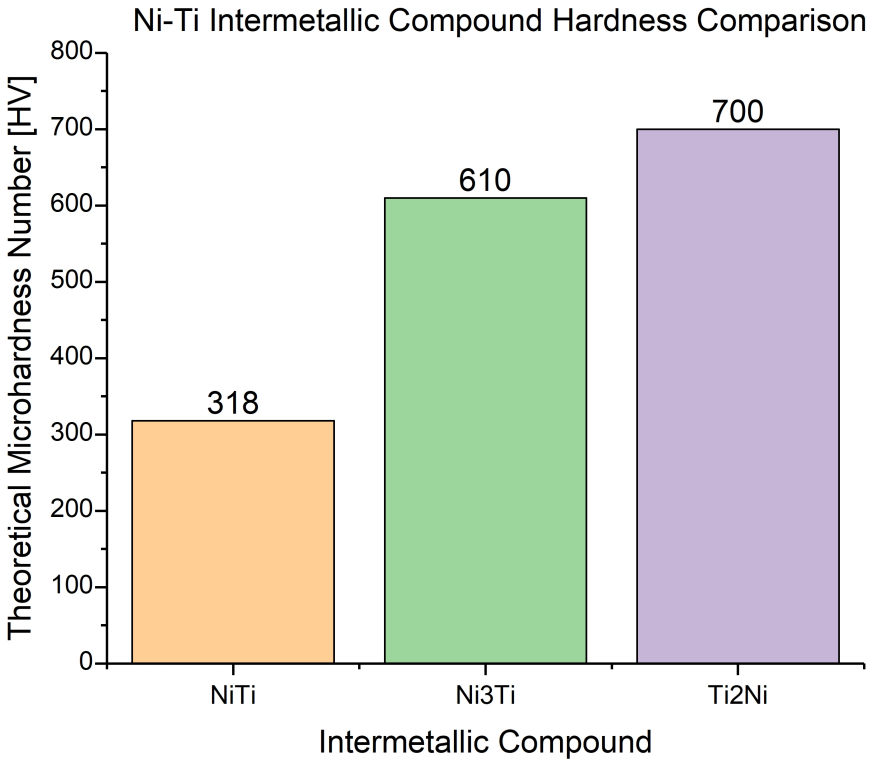

FIGURE 2.1: Theoretical microhardness values of Ni-Ti intermetallic compounds Man et al. [2006], Reddy et al. [2018], Gao and Wang [2008]

2.3 Electrolytic Plasma Processing

Electrolytic Plasma Processing and Plasma Electrolytic Oxidation fall under the umbrella of Plasma Electrlyte Deposition (PED), an area of research that has become quite active in recent years. EPP/PEO boasts high deposition rates, environmental cleanliness, a lack of harsh and dangerous chemicals, and deposition of metallics, ceramics, as well as oxide creation.

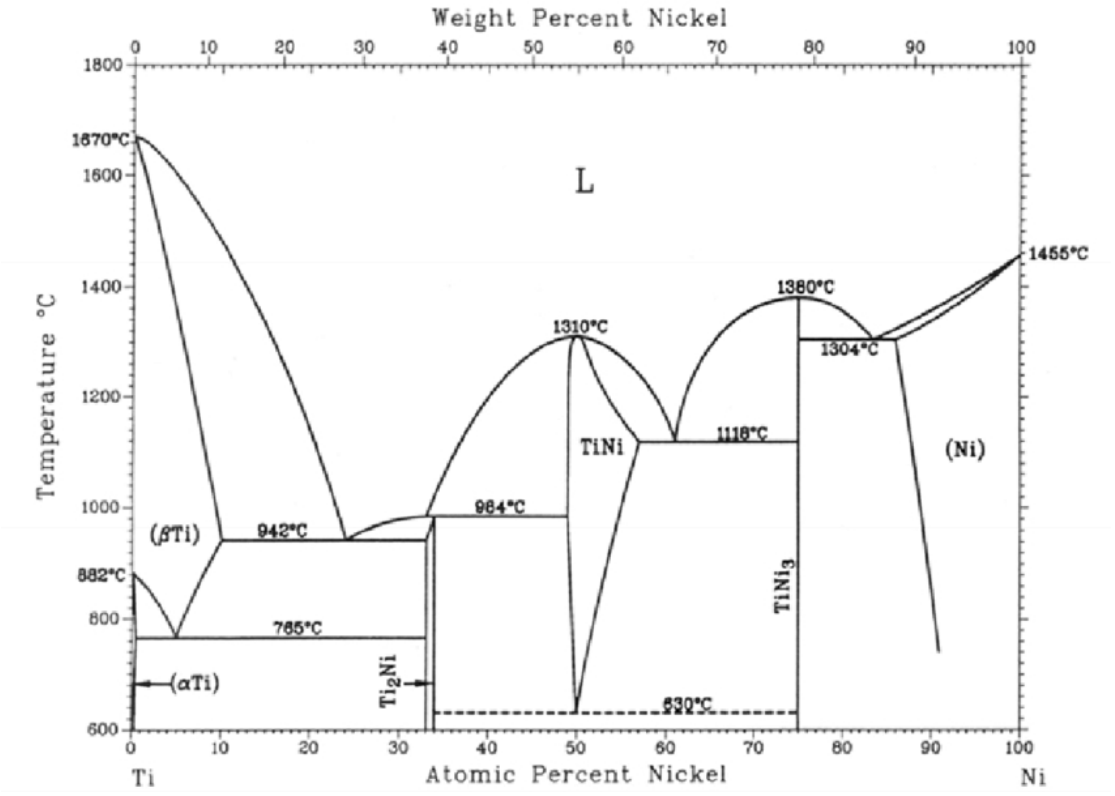

FIGURE 2.2: Equillibrium phase diagram of Ti-Ni alloys Batalu et al. [2020]

The EPP process utilizes an aqueous electrolyte that forms a conductive bridge between work piece and counter-electrode. Depending on polarity, the process can be used for deposition or oxide building. Treating the workpiece as the anode induces non-metallic deposition (oxides, sulfides, etc. Barati [2018], Fattah-alhosseini et al. [2020], Nikoomanzari et al. [2020], Mortazavi [2017]) while treating the workpiece as the cathode induces metallic deposition and surface cleaning (Meletis et al. [2002], Smith [2014], Gupta et al. [2007], Aliofkhazraei and Roohaghdam [2007]). This study focuses on the cathodic polarity of the EPP process for the deposition of Ni on pure Ti.

In cathodic EPP deposition, there exists 4 phases of current density response to voltage increase. In phase 1, shown as U_1 in Figure 2.3, current density increase linearly with voltage according to Ohm's Law ($V = IR$). During the linear growth of current density, electrolysis of water occurs, creating gaseous evolution of H_2 within the envelope of

the electrolyte and on the workpiece surface following the cathodic reaction detailed in Equation 2.1:

$$2H^{+}(aq) + 2e^{-} \rightarrow H_2(gas) \tag{2.1}$$

In phase 2 of the EPP process (U_2 in Figure 2.3), luminous flashes occur with further voltage increase and instability ensues in the current density. At this point, the current density will find a maximum value, but will remain unstable untill further increase in voltage. During this instability, Joule heating of the solution occurs concentrated around the cathode workpiece, locally increasing the electrolyte temperature within the envelope formed between electrodes. This Joule heating effect is accompanied by a marked increased in electrolyte conductivity according to Equation 2.2 and 2.3 Paulmier et al. [2007]:

$$\Delta T(t) = \frac{\int_{t}^{t+\delta t} V(t`) \times I(t`)dt`}{v \times \rho \times C} \tag{2.2}$$

$$(\sigma(T + \Delta T)) = \sigma(T) + \alpha_t \times \Delta T \tag{2.3}$$

where v is the solution volume in the working envelope, ρ is the solution density in the same region, σ represents the conductivity of the electrolyte, and α_t is a constant over the temperature range of 270K-350K. Paulmier et al. [2007] definitively showed this conductivity increase in the envelope, suggesting an approach to the vaporization temperature of the electrolyte within the envelope acting as the driving mechanism for the nucleation of hydrogen bubbles on the workpiece surface.

In phase 3 of the EPP process (U_3 in Figure 2.3), we see a substantial drop in current density as voltage continues increasing in a linear fashion. The minimum current density occurs swiftly after the marked current drop in this phase, sometimes instantaneously. This is where a continuous plasma envelope has formed between electrodes and the sample surface is immersed in plasma. The minimum current density of this phase allows for control of the plasma features and allows for repeatable processing of sample surfaces. This is the phase in which EPP deposition occurs.

Increasing voltage further induces phase 4 of the EPP process (U_4 in Figure 2.3) in which current density begins another unstable phase. As voltage increases, current density begins to climb once again, and the plasma envelope becomes uncontrollable. This is dubbed the arcing regime as voltage and current density increases induce violent plasma arcs that destroy the sample surface Smith [2014], Paulmier et al. [2007], Gupta et al. [2007], Aliofkhazraei and Roohaghdam [2007].

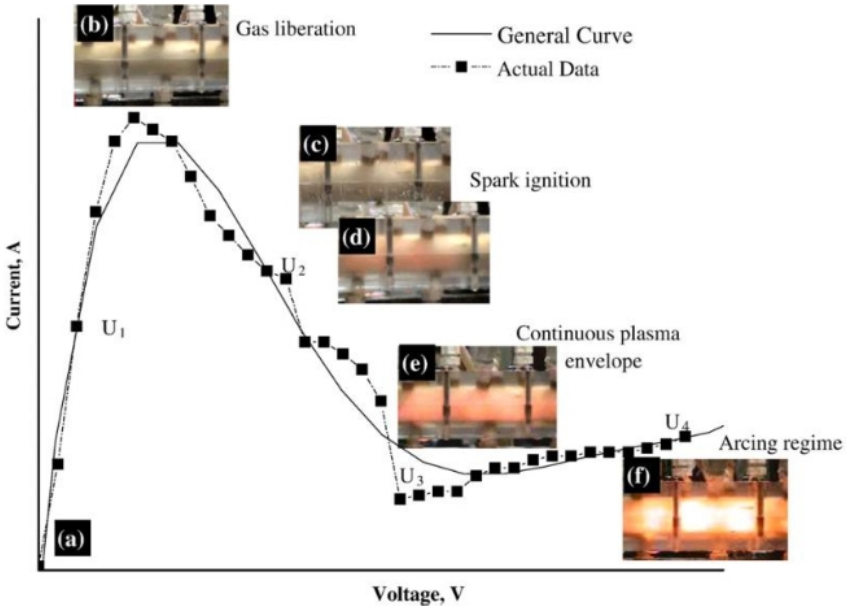

FIGURE 2.3: Typical full I-V response of the EPP process Gupta et al. [2007]

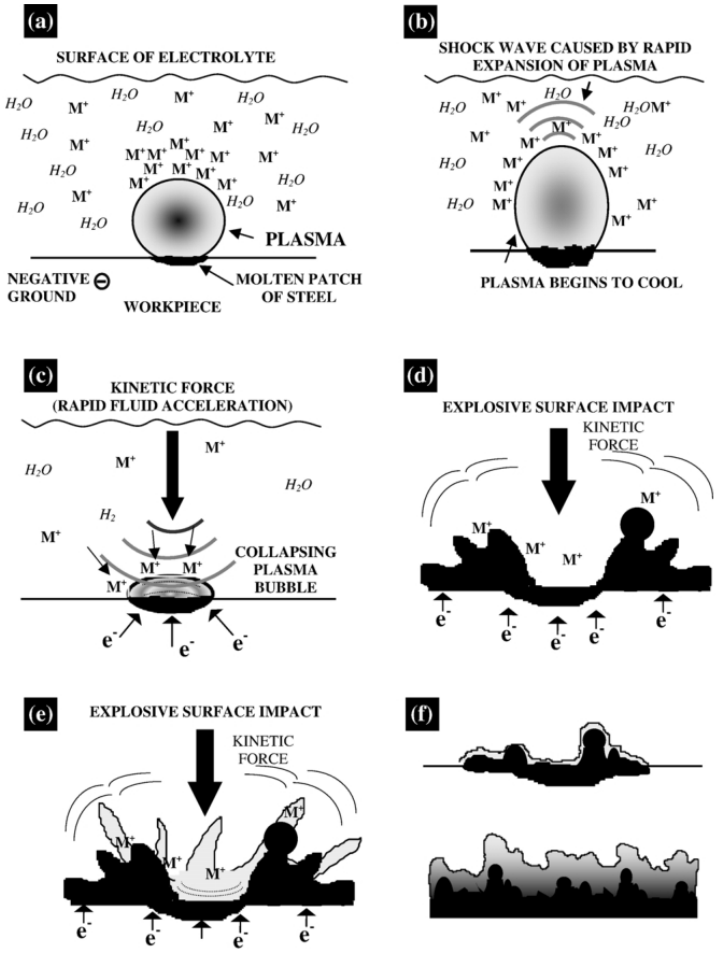

FIGURE 2.4: Depiction of hydrolysis and hydrogen bubble formation in EPP Gupta et al. [2007]

In an EPP desposition process, hydrolysis of the electrolyte causes the liberation of gaseous H_2 bubbles on the workpiece surface. Due to the electric field present between the workpieces, ionic species from the electrolyte are attracted to the sample surface according to the Coulombic Force. By this point in the process, the entirety of the sample is enveloped in a vapor plasma sheath, causing a drastic rise in surface temperature of the substrate along with a seperation of the surface and conductive bridge, causing the U_3 current density drop almost instantaneously. Surface temperature of the substrate has been estimated to be between 2000K and 6000K at an given moment, not accounting for thermal fluctuation locally Smith [2014], Gupta et al. [2007], Paulmier et al. [2007]. Due to electrostatic pressure gradients as well as continous bombardment of electrolyte,

the pressure within the hydrogen bubbles differs greatly from that of the surrounding plasma medium. This pressure gradient causes significant and rapid reshaping of the plasma and bubble surface, leading to an eruption of the bubble and an ensuing shockwave. The kinetic force driven by hydrogen bubble collapse and shockwaves implants ionic species into the molten surface of the substrate. During this process, the surface of the substrate is continuously melted by high temperature plasma and refrozen by flowing electrolyte. This continuous melting and refreezing process in conjunction with bubble-shockwave kinetics induces a microcraterous surface morphology and layered intermetallic formation. Due to the rapidity of quenching, certain metastable intermetallic compounds and high temperature phases may be formed in layers throughout the film. The estimated life of bubbles during this process is approximately 1μs Meletis et al. [2002].

The resultant coatings from EPP metallic deposition are always microcraterous and protruding nanospheroids, and generally boast a consistent nanograin structure. In order to understand the EPP process it is important to understand the dynamics of the necessary plasma. While a consistent plasma envelope forms between electrodes, the plasma interaction at the workpiece surface is not a consistent envelope. The collapse and kinetics of hydrogen bubbles suggests that plasma interaction at the surface occurs in discreet layers, further supported by the layered structure of intermetallic compounds created near the interface of coating and substrate as well as throughout the film Yerokhin et al., Paulmier et al. [2007].

Chapter 3

Experimental Methods

3.1 Materials

Necessary materials for deposition utilizing the EPP process include the workpiece substrate and the deposition media, i.e. the work electrolyte. Substrates are cut from commercially pure Ti into cylinders with a diameter of 9.95 mm (0.392 inch) and a height of 8.96 mm (0.353 inch). The substrate is suspended in the processing chamber by a copper rod threaded to #8-32, therefore a #8-32 hole is tapped into the rounded side of the cylinder. Initially the tapped hole was centered on the rounded side of the cylinders but was later moved toward the bottom of the cylinder to reduce interaction with the copper rod holder and the counter electrode above. All substrates were polished with 320 grit, 400 grit, 600 grit, 800 grit, 1000 grit, and 1200 grit SiC polishing paper in successive order to ensure a surface roughness no greater than 100 nm before processing. Polished samples are washed with methanol, dried, and then wrapped in 6 to 7 layers of insulating tape so as to leave only the polished work surface exposed to the process.

The electrolytes used in the EPP process vary based on polarity and desired outcome. The cleaning process is done using $NaHCO_3$ at a concentration from 10% to 20% depending on desired surface morphology. The effect of concentration on surface morphology is discussed in a later section. For the deposition of nickel, a nickel rich solution is created with 20% $NiSO_4$ mixed in DI water. The process is completed at an electrolyte temperature of 75°c, resulting in an electrolyte conductivity of 47 mS/cm and 3.7 pH. Changes in processing temperature appear to have little effect on resultant coatings, however temperatures lower than 65°c were incapable of producing the necessary plasma for processing, therefore 75°c is chosen for consistency in conductivity and pH, and therefore reliability in plasma production.

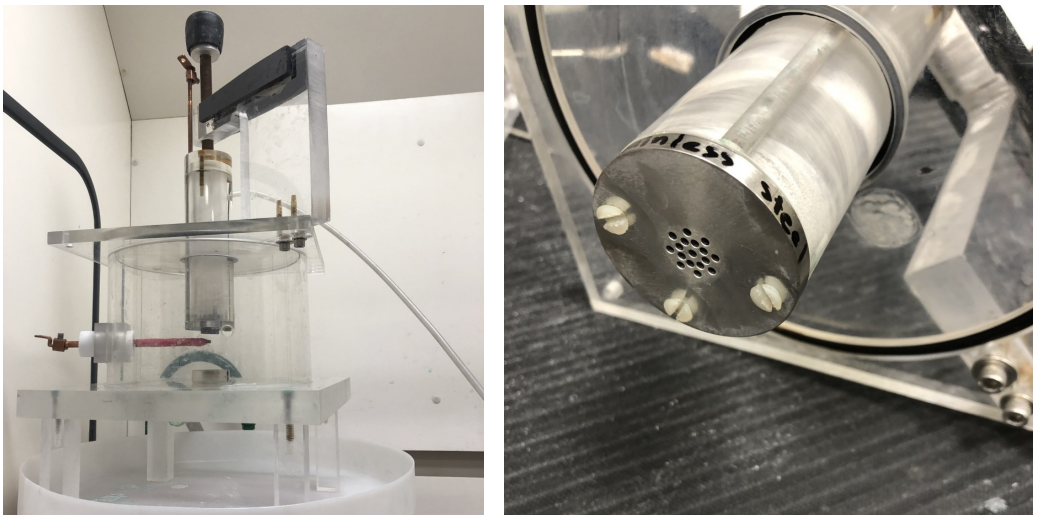

(a) (b)

FIGURE 3.1: SaNEL EPP chamber and stainless steel counter electrode

3.2 Electrolytic Plasma Processing

The chamber used for EPP is a clear arcylic plastic cylinder with a drainage hose, a #8-32 threaded copper mounting rod, and a removeable lid equipped with an electrolyte intake location and an adjustable threading for raising and lowering the counter electrode. The

counter electrode is a 307 stainless steel flattened cylinder 50.8 mm (2 inches) in diameter and 0.24 mm (0.009 inches) in height. The electrode has 3 concentric rings of holes 1.905 mm (0.075 inches) in diameter to be centered above the workpiece. During the process, the electrolyte flows into the system via the intake location in the lid and flows down through the counter electrode and onto the workpiece. Several workpieces exist and may be used in the system including Ni, Ti, Mo, Zn, Al, and graphite. It is unclear if material is removed from the anode and deposited onto the workpiece during the EPP process, however the change in conductivity between electrode materials seems to affect plasma creation. Polished and wrapped substrates are screwed onto the copper mounting rod, centered in the chamber by adjusting the fastening screw holding the mounting rod, rotated such that the substrate surface and the counter electrode are parallel, and the counter electrode is raised such that the working distance between electrode and work piece is 5 mm. The counter electrode and workpiece (via copper mounting rods) are attached to a Sorrensen SGA 600-17 power supply rated for 10 kW power output and maximums of 600 V and 17 A. The copper mounting rods are periodically cleaned and polished to ensure good electrical contact with work pieces. At the time of experiment, the copper rods boast a resistance of 0.01 Ω. The electrolyte is continuously pumped through a centrifuge pump at a maximum flow rate of 2L/min, with an inline valve near the chamber intake for flow rate adjustment. Experiments in this work have been conducted with a flow rate of 2L/min unless clearly stated otherwise. Data in each experiment is gathered with a Tektronix TDS 2000C Series oscilloscope equipped with a 10mA/V to 100mA/V loop-current reader.

Deposition of Ni on Ti was conducted at a working distance of 5mm with a processing voltage of 190 V resulting in a processing current density between 1.5 A/cm^2 and 4.0 A/cm^2, with a maximum current density of 18.2 A/cm^2. Once the $NiSO_4$ electrolyte

reaches 75°c, the pump is turned on and the electrolyte flows through the counter electrode and forms a conductive bridge to the substrate. A full current vs. voltage response is generated from 0 V to 250 V to determine the proper processing voltage, i.e. the voltage resulting in the minimum stable current density. Upon determining the processing voltage, samples were processed for 10s, 20s, and 30s to determine the growth rate of EPP deposited films. After processing the samples are washed in an ultrasonic ethanol bath to remove corrosive electrolyte left from the process, as well as, any remnants of insulating tape, adhesive, or excess material that did not integrate into the coating.

3.3 Methods of Analysis

Analysis of these samples was conducted in the UTA CCMB (Characterization Center for Materials and Biology). The surface of each sample has been analyzed for surface roughness and topography via optical profilometry, surface morphology and macro defects via scanning electron microscopy (SEM), crystalline phases via X-ray Diffraction Spectroscopy (XRD), and atomic weight concentration at the coating surface via Energy Dispersive Spectroscopy (EDS). Analysis of the coating structure is conducted by cross sectioning the samples. A small slice of the sample is cut off such that the coating lay exposed. The cut is then mounted in a hot press bakelite mount so as to protect the coatings integrity, and polished up to 1000 grit. Coating bulk morphology and thickness are studied via SEM, and an EDS linescan is used to determine the change of atomic weight percentage throughout the film. In order to study intermetallic formation at the interface of coating and substrate, a foil (10 microns in thickness) was cut, polished, prepared and analyzed for use in a Transmission Electron Microscope (TEM) to study

grain size, grain orientation, and gather crystal structure information for various phases formed at the interface and coating.

3.3.1 Optical Profilometry

Optical profilometry was conducted in the SaNEL laboratory using the Veeco NT9100 Optical Surface Profilometer. This tool was utilized to determine the pre-process roughness, as well as the roughness of each coating's surface. The scanning region while using the 5x aperture is aproximately 1.3 mm x 0.95 mm. Samples were not processed with roughness exceeding 100 nm according to these tests.

$$R_a = \frac{1}{n}\sum_{i=1}^{n} \mid y_i \mid \tag{3.1}$$

Equation 3.1 is used to find the surface roughness of a sample measured via optical profilometry.

3.3.2 SEM and EDS

Scanning Electron Microscopy images were taken using a Hitachi S3000N SEM. Measurements were taken with an accelerating voltage of 25 kV and a working distance of 15 mm. Surface morphology and cross section morphology were both acquired utilizing this machine. Additionally, an EDS attachment is utilized on the same microscope to determine surface atomic weight percentage and bulk atomic weight percentage via linescan.

3.3.3 XRD

X-ray Diffraction Spectroscopy data were taken using a Bruker D8 Advance X-ray Diffractometer. Measurements were taken with an accelrating voltage of 40 kV and an accelerating current of 40 mA. The radiation source for all measurements was a Cu Kα source boasting a wavelength of 1.54 Å. All analysis was conducted in θ-2θ mode with a step size of 0.01 degrees and a scan dwell time of 1 second.

$$\tau = \frac{K\lambda}{\beta cos(\theta)} \tag{3.2}$$

Equation 3.2 is the Scherrer equation used to estimate the sub-micro grain size via XRD data.

3.3.4 TEM

Transmission Electron Microscopy images were taken using a Hitachi H-9500 High-Resolution TEM with an accelerating voltage of 300 kV boasting a resolution of approximately 0.18 nm. This machine also utilizes an EDAX EDS for elemental analysis of single grains or very minute sections of the interface. X-Ray diffraction data was also measured for individual grains and minute sections of the interface. Samples were cut into a cross section slice, polished on both sides to 1200 grit and a thickness of approximately 100 microns before being mounted, polished on the measurement side with microplaten to approximately 30 microns, polished with a dimple grinder to approximately 15-20 microns, and ion polished to approximately 10 microns.

3.3.5 Microhardness

Microhardness data is taken with a LECO LM 300 AT Microindenter equipped with a Vicker's diamond tip and indention tool capable of loads from 10gf to 200gf. Measurements on this machine are taken via a 50X objective optical microscope. In order to maintain accuracy and precision, and to establish some statistical analysis, microindentation measurements are checked with the SEM. SEM indent measurements matched optical indent measurements to approximately 0.25μm. The calculation of Vicker's hardness number is conducted with Equation 3.3:

$$HV = 0.1891\frac{F}{d^2} \tag{3.3}$$

Where F is the load supplied and d is the diagonal measure of the diamond indent.

3.3.6 Corrosion Testing

Corrosion testing is conducted in the UTA SaNEL laboratory in varied setups depending on test parameters (aerated, deaerated, etc.). This thesis includes anodic polarization data to determine the corrosion potential and the corrosion rate of deposited EPP thin films. These tests were conducted by applying voltage to the sample that is submersed in corrosive media in close proximity to a saturated calomel reference electrode.

Chapter 4

Ni deposition on Ti via EPP

4.1 Introduction

Many early experiments were performed with parameters based upon literature and experimentation performed by previous SaNEL researches on similar EPP projects, i.e. Smith [2014], Cionea [2010], Barati [2018], Mortazavi [2017], as well as current researches findings that have yet gone unpublished. However, experimental parameters immediately became difficult to compare as only one configuration of the EPP chamber could reliably produce plasma stable enough to create coatings with any adhesion and lack of arcing damage.

4.1.1 Effect of counter-electrode material

The initial experiment when changing any variable in the procedure are full I-V curves in order to determine a processing voltage. If initial I-V processes fail to produce viable plasma, they are repeated with a varied rate of voltage increase. Table 4.1 shows the effects of changing the counter-electrode material.

"Electrode Material"	Spout/Flat	Concentration	"Processing Temp."	Pass/Fail
"Stainless Steel"	Spout	0.1	75	Fail
"Stainless Steel"	Spout	0.15	75	Fail
"Stainless Steel"	Spout	0.2	75	Fail
"Stainless Steel"	Spout	0.2	70	Fail
"Stainless Steel"	Spout	0.2	80	Fail
"Stainless Steel"	Flat	0.07	75	Fail
"Stainless Steel"	Flat	0.1	75	Fail
"Stainless Steel"	Flat	0.15	75	Pass
"Stainless Steel"	Flat	0.2	75	Pass
"Stainless Steel"	Flat	0.2	70	Fail
Titanium	Spout	0.1	75	Fail
Titanium	Spout	0.15	75	Fail
Titanium	Spout	0.2	75	Fail
"Graphite WHOLE"	Spout	0.1	75	Fail
"Graphite WHOLE"	Spout	0.15	75	Fail
"Graphite WHOLE"	Spout	0.2	75	Fail
Graphite/Stainless	Spout	0.1	75	Fail
Graphite/Stainless	Spout	0.15	75	Fail
Graphite/Stainless	Spout	0.2	70	Fail
Graphite/Stainless	Spout	0.2	75	Fail
Graphite/Stainless	Spout	0.2	80	Fail
Aluminum	Flat	0.1	75	Fail
Aluminum	Flat	0.15	75	Fail
Aluminum	Flat	0.2	70	Fail
Aluminum	Flat	0.2	75	Fail
Aluminum	Flat	0.2	80	Fail

TABLE 4.1: Details of inability to produce viable plasma with various materials of electrode. Experiments marked with "Fail" that were repeated with varying voltage increase rates but still failed all attempts are only marked once.

Several aspects of the counter electrode piece have been studied to determine effect on the EPP process. In early experiments, the EPP cleaning process was studied for training purposes and ensuring the functionality of the machine. All cleaning processes were carried out with $NaHCO_3$ electrolyte at 20% concentration with a graphite spout electrode threaded into a stainless steel holder. This setup proved non-functional for Ni deposition on pure Ti substrates as no plasma was able to be produced at any electrolyte concentration. At each tested concentration, experiments were conducted with varied rates of voltage increase, as well as varying working distances. As a result, each variable was isolated and tested with several different electrode materials. To test electrode hole

size, and by extension electrolyte flow rate, tests were conducted at 7%, 10%, 15%, and 20% $NiSO_4$ concentration with a working distance of 5 mm with the graphite spout in steel holder, whole graphite spout, whole stainless steel spout, and whole titanium spout, all of which have the same hole symmetry and size. None of these tests, at any voltage increase rate (i.e. 5 V/sec., 15 V/sec, 20 V/sec., 50 V/sec.), produced viable plasma for deposition. Next, the effect of counter electrode shape was tested along with material. All tests were repeated at varied concentrations and voltage increase rates with a flat stainless steel, flat graphite, and flat aluminum counter electrode. Only the flat stainless steel electrode was capable of producing a viable plasma consistently.

4.1.2 Effect of Electrolyte Concentration

As has already been noted, substantial testing of electrolyte concentration has been undertaken to determine the effect, if any. While difference in electrolyte concentration during the cleaning process has been studied and documented by several SaNEL researchers (Smith [2014]), no such relationship was able to be determined during the Ni deposition on pure Ti process. In the cleaning process, lower concentration electrolytes contain far fewer conductive species for carrying current through the electrolyte bridge to facilitate plasma creation. As a result, a far greater voltage must be supplied to induce a critical current and in turn induce electrolysis of hydrogen. Thus, as noted by Smith et al., greater surface damage and inferior coverage can be induced. This effect is detrimental for surface coating thickness, adhesion, and morphology. When studying variation of $NiSO_4$ concentration in the Ni deposition process, stable plasma could not be achieved before arcing occured with electrolyte concentration below 20%. The voltage and current density would increase linearly until a spontaneous and violent plasma

arcing event occured at 225-235 V. For reference, at 20% concentration, arcing events begin quite mildly around 220-230 V, and become destructive up to 250 V.

4.2 Characterization of Ni Deposited Pure Ti

The processing voltage of the Ni deposition process was determined by producing a full I-V response up to 250 V, well into the arcing regime. As expected from literature and theory, current density increases linearly with voltage before going through an instability regime as hydrogen electrolysis beings. After this instability is passed with further voltage increase, the processing voltage is reached where current density is minimized.

4.2.1 I-V Response

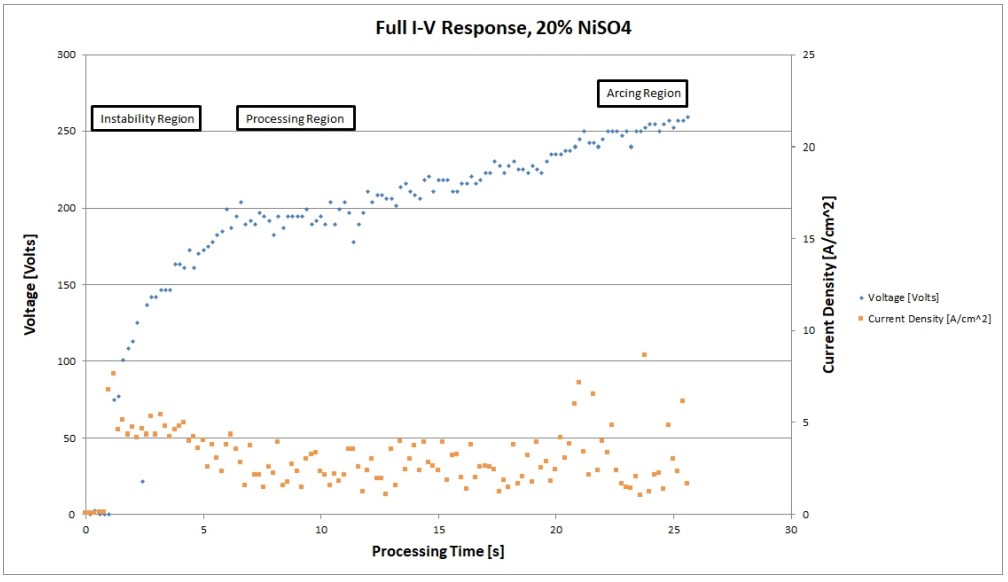

FIGURE 4.1: Full I-V response of 20% $NiSO_4$ electrolyte in Ni deposition on Ti

Initial sparking can indicating the onset of sample surface damage is observed to begin at approximately 210 V, with violent arcing clearly displayed at voltages exceeding 230 V.

With a processing voltage and expected current density selected, i.e. 190 V - 200 V, samples were processed for 10s, 20s, and 30s to determine film growth rate and effect of processing time on surface morphology, elemental weight percentage, microstructure of the bulk and the interface, and the presence of Ni-Ti intermetallics.

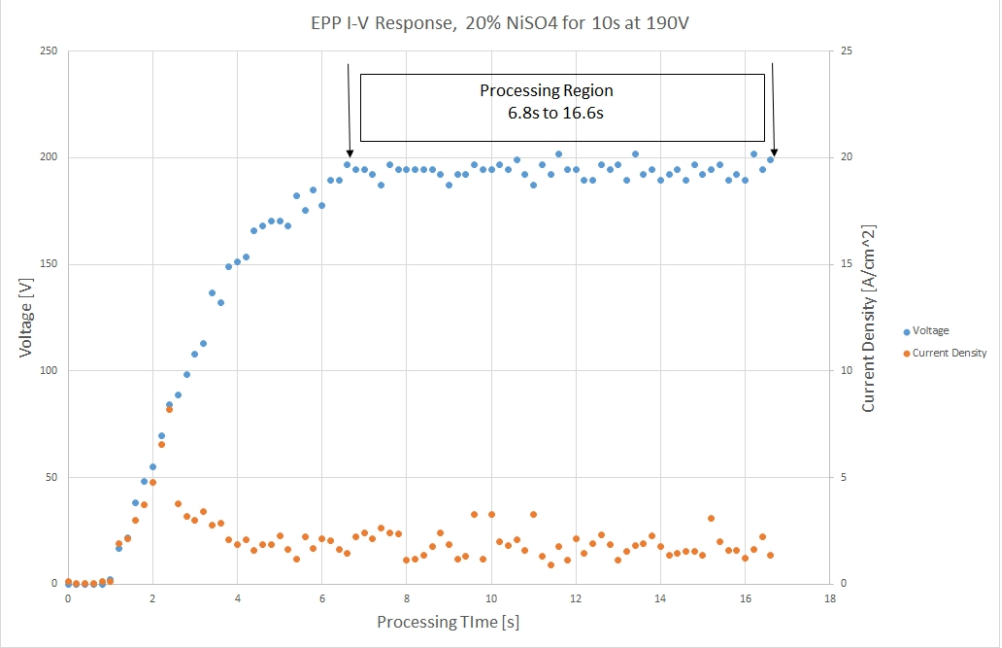

FIGURE 4.2: 10s deposition of Ni on Ti at 190V

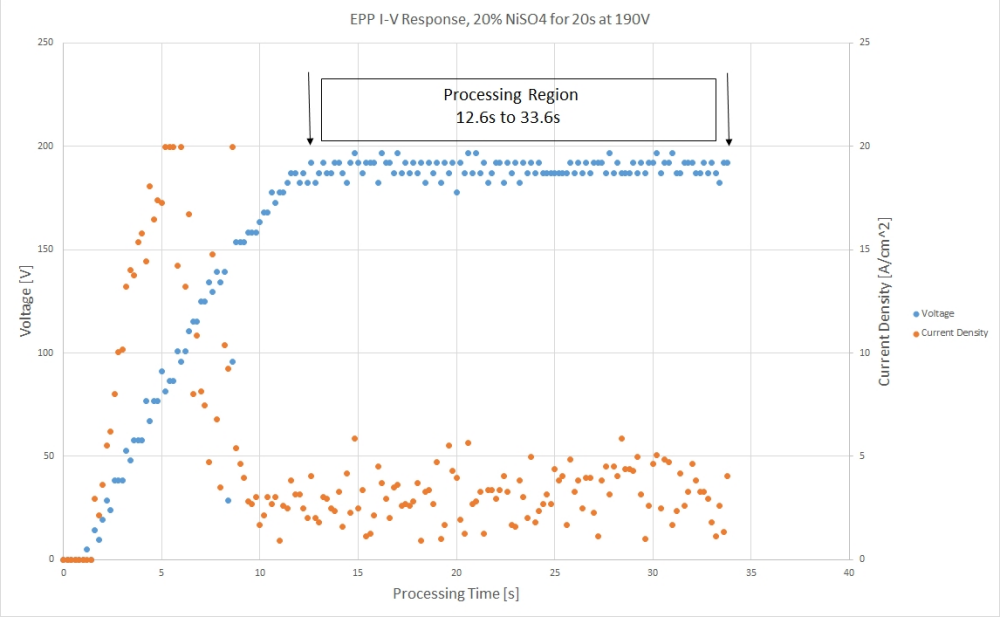

FIGURE 4.3: 20s deposition of Ni on Ti at 190V

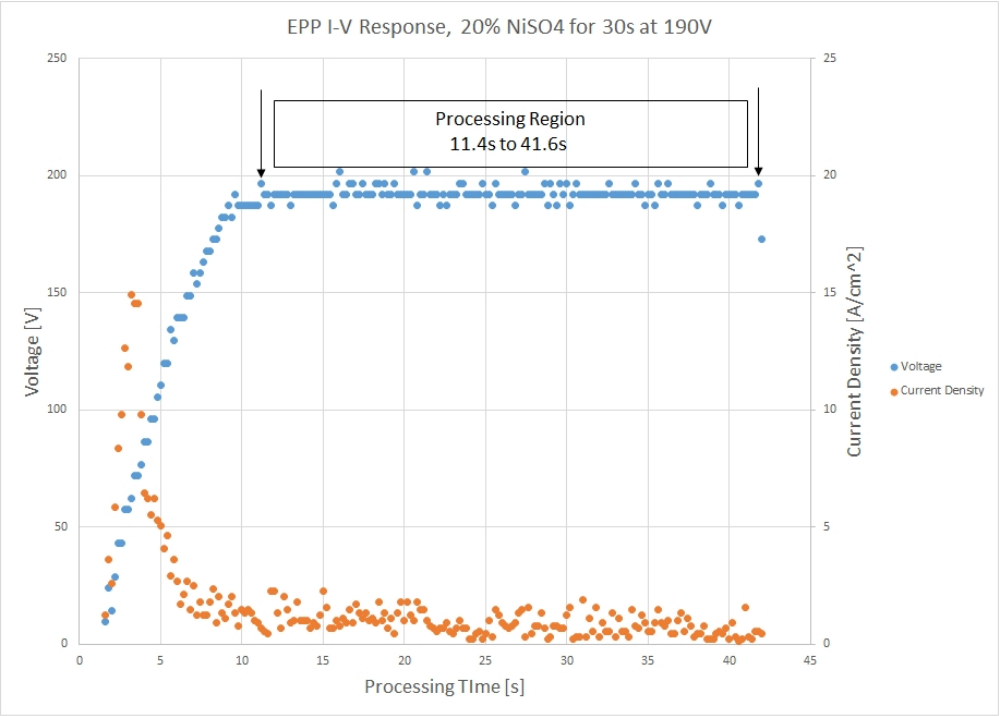

FIGURE 4.4: 30s deposition of Ni on Ti at 190V

4.2.2 Surface Morphology

Utilizing the Hitachi S3000N SEM with an accelerating voltage of 25 kV and a working distance of 15 mm, surphace morphology observations were made to ensure the expected micro-craterous appearance could be found. As expected, more processing results in a more craterous surface due to more material for deposition as well as more mixing. In Figures 4.5, 4.6, and 4.7, it is clear to see that the surface structures (i.e. microcraters) consistently increase in size and are more closely packed. While this results in a rougher surface, it is clear that the process is successfully depositing layer upon layer of pure Ni onto the surface of Ti substrates as desired.

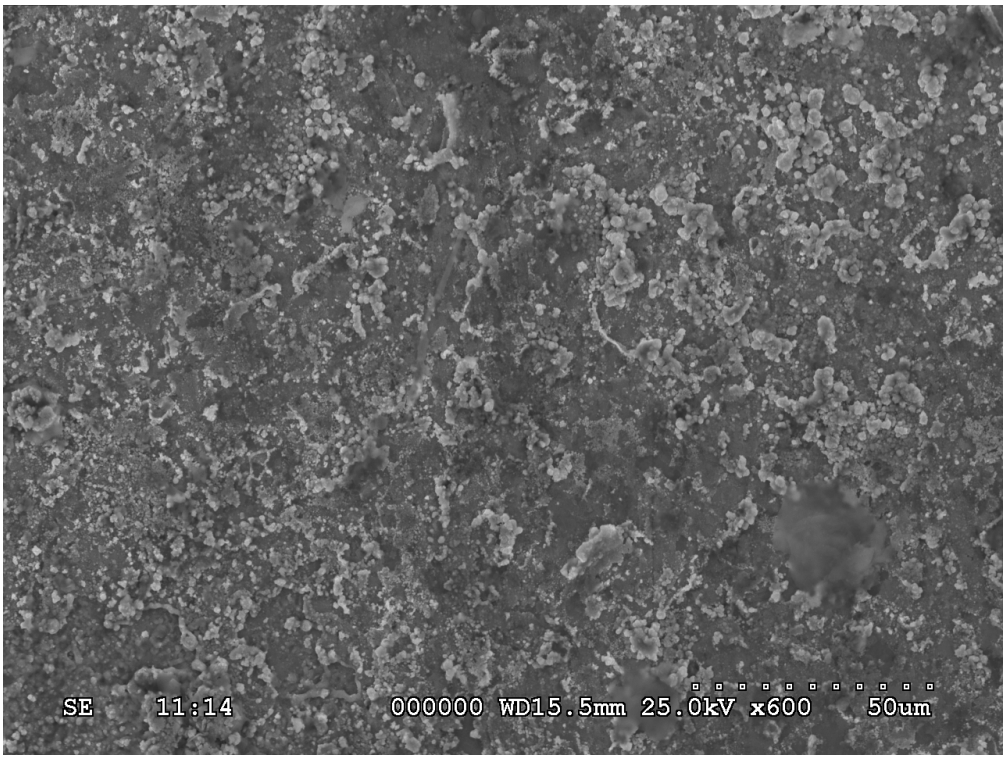

FIGURE 4.5: SEM surface image of 10s Ni deposition via EPP, 600x magnification

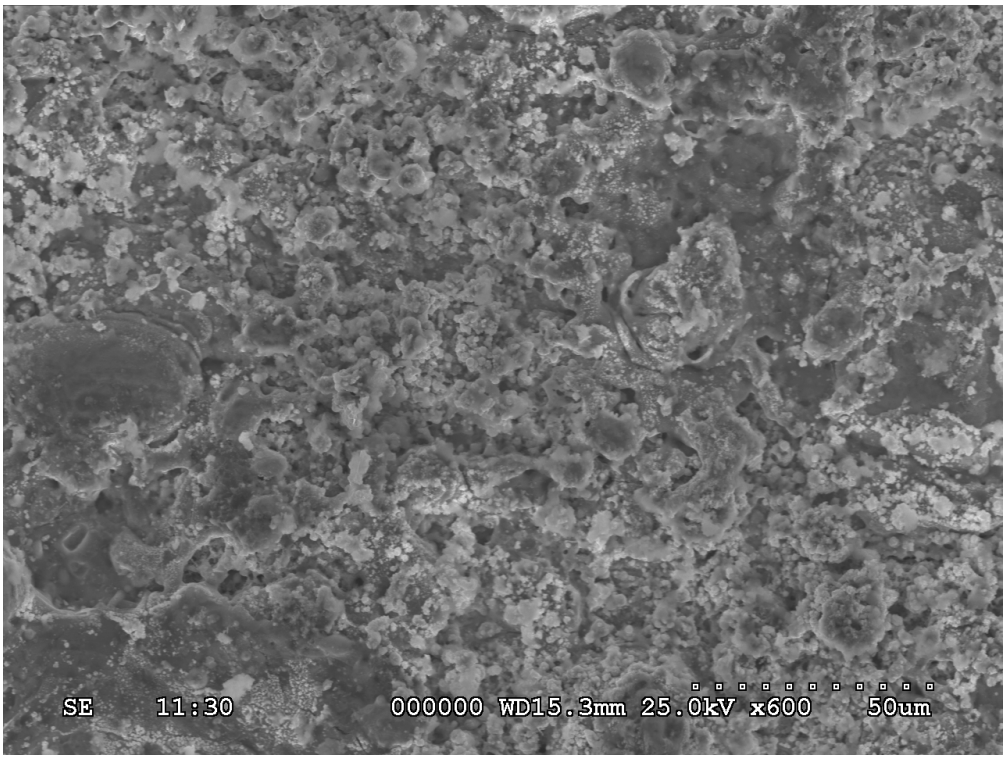

FIGURE 4.6: SEM surface image of 20s Ni deposition via EPP, 600x magnification

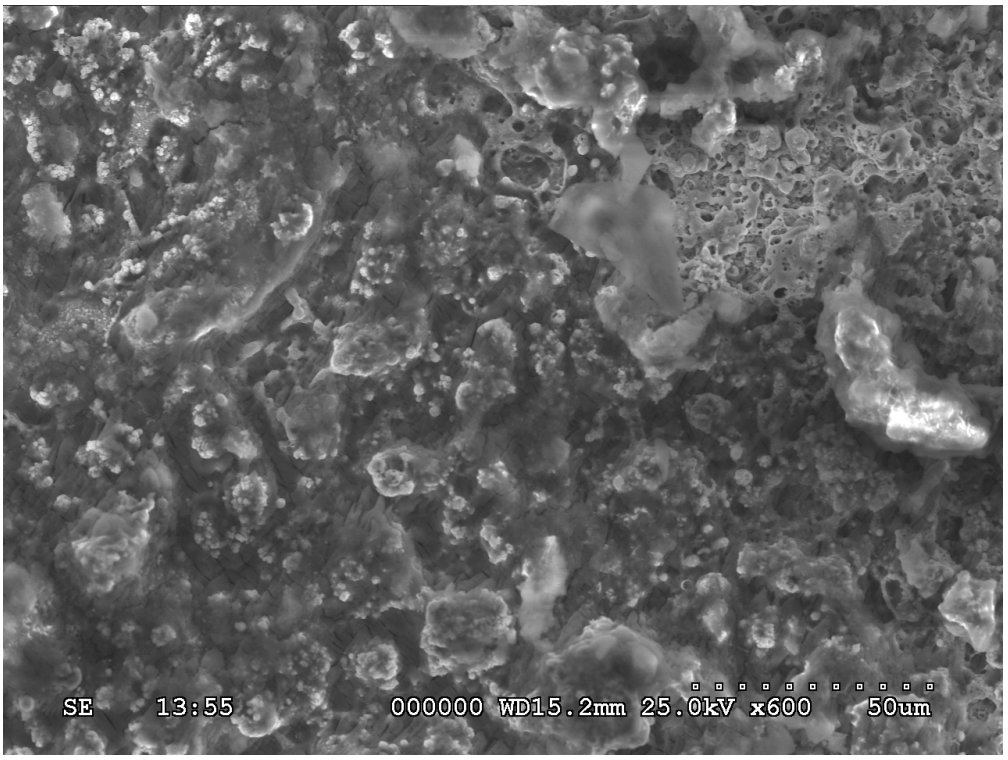

FIGURE 4.7: SEM surface image of 30s Ni deposition via EPP, 500x magnification

4.2.3 Surface Roughness

All samples were polished to surface roughnesses not exceeding 100 nm before processing to ensure a smooth and uniform surface for coating. The roughnesses of resultant coatings are analyzed to determine a relationship between post process surface roughness and processing time. As expected, due to the cyclical melting and re-freezing process, longer processing times result in much rougher films. While this trend must be confirmed with longer processing times, it appears that maximum surface roughness begins to taper off with greater processing times.

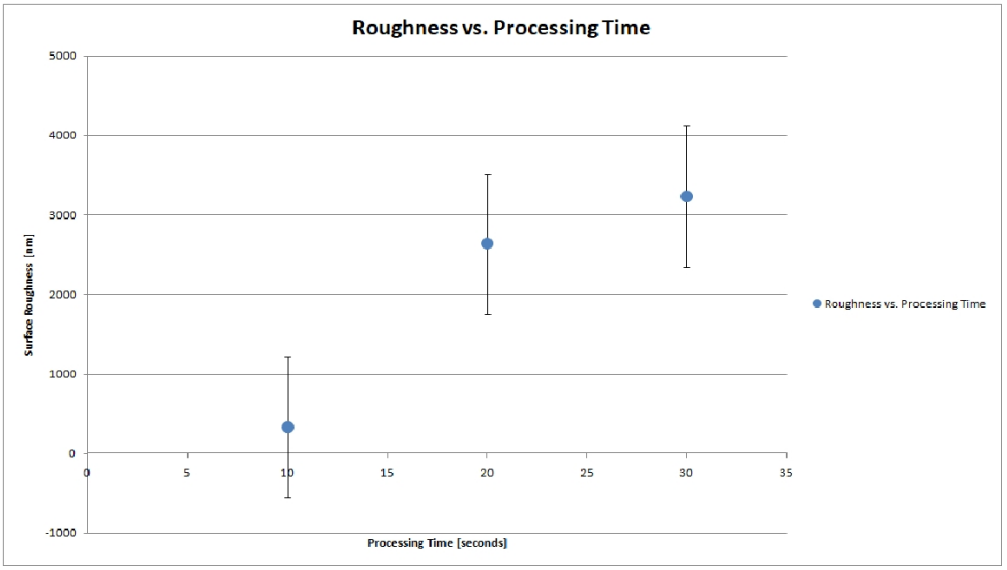

FIGURE 4.8: Optical profilometry measurements of surface roughness as a function of processing time

4.2.4 Surface Microstructure

X-Ray Diffraction is utilized to determine the existence of Ni-Ti intermetallics from the melting and refreezing process in EPP deposition, as well as to determine the pure Ni and Ti phases displayed in functional coatings.

As expected, pure Ni and pure Ti are discovered via XRD. Ti seen by XRD suggests a gradient of mixing through the film, as well as some penetration of x-rays into the bulk of the film. Notice that peaks appear broadened and substantial shoulders can be found, which leads to the conclusion that there may be intermetallic responses nearby. Table 4.2 shows the possible intermetallic peaks that may be broadening pure Ti and pure Ni peaks. By the Scherrer Equation, deposited Ni grains are estimated at approximately 76 nm, well within the the expected nanograin size dictated by the melting and refreezing process of EPP deposition. As deposition time increases, Ni peaks become stronger and sharper, indicating expected presence of pure Ni at the film surface, and a higher percentage of Ni on a gradient through the film from substrate to surface.

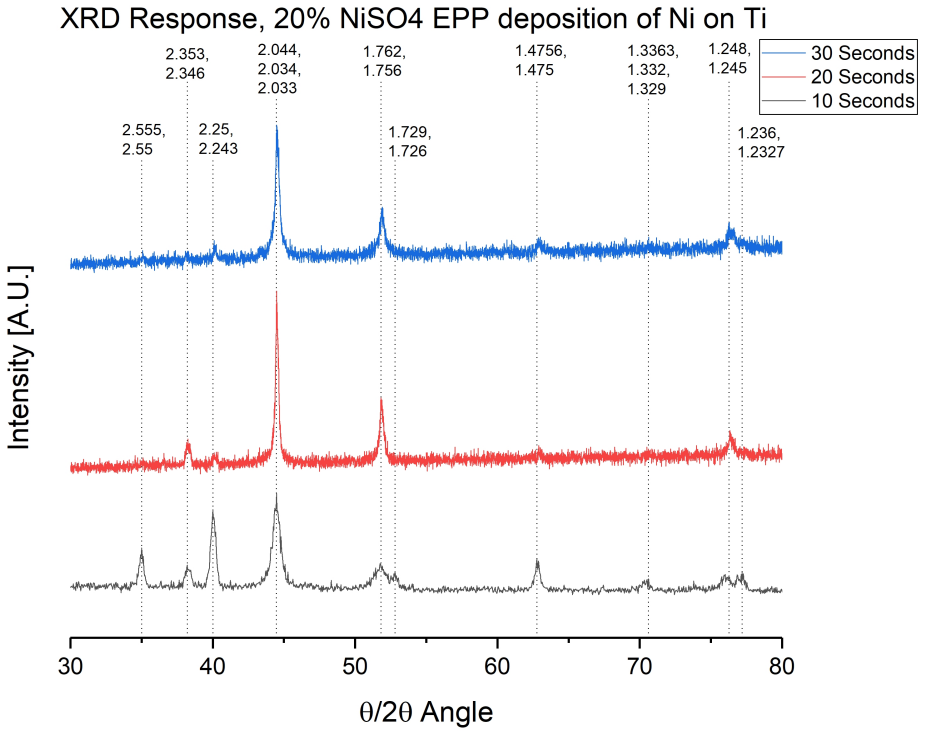

FIGURE 4.9: XRD Intensity vs. 2θ response of 10s, 20s, and 30s EPP Ni depositions on Ti

TABLE 4.2: Corresponding measurements and theoertical values to the XRD spectra shown in Figure 4.9

Peak	d Spacing [Å] Theory	d Spacing [Å] Measured)	Material	$\theta 2\theta$ [Degree]	Plane
1	2.555	2.63	Ti Hex.	35.093	(100)
	2.55	2.63	Ni_3Ti Hex.	35.157	(110)
2	2.353	2.34	NiTi Mono	38.21	(110)
	2.346	2.34	Ni_3Ti Hex	38.334	(103)
3	2.25	2.244	Ni_3Ti_4 Rhombo.	40.026	(202)
	2.243	2.244	Ti Hex.	40.17	(101)
4	2.044	2.022	Ni_3Ti_4 Rhombo.	44.275	(23$\underline{1}$)
	2.034	2.022	Ni FCC	44.493	(111)
	2.033	2.022	Ni Hex.	44.52	(011)
5	1.762	1.759	Ni FCC	51.846	(200)
	1.756	1.759	Ni_3Ti_4 Rhombo.	52.014	(042)
6	1.729	1.731	Ni_3Ti_4 Rhombo.	52.894	(241)
	1.726	1.731	Ni_3 Ti Hex.	52.987	(203)
	1.726	1.731	Ti Hex.	53.004	(102)
7	1.4756	1.495	Ni_2Ti Rhombo.	62.934	(1 0 22)
	1.475	1.495	Ti Hex.	62.949	(110)
8	1.3363	1.336	Ni_2Ti Rhombo.	70.402	(0 1 26)
	1.332	1.336	Ti Hex.	70.66	(103)
	1.329	1.336	Ti_2Ni FCC	70.844	(660)
9	1.248	1.249	Ti Hex.	72.218	(112)
	1.245	1.249	Ni FCC	76.376	(220)
10	1.236	1.233	NiTi Mono.	77.102	(130)
	1.2327	1.233	Ni_2Ti Rhombo.	77.349	(119)

4.2.5 Cross Section Analysis

Samples were cut and mounted to analyze the morphology, elemental analysis, and thickness of EPP coated films. SEM images have been generated to study the morphology of the coating and interface, while cross-section EDS is used to determine the elemental proportions throughout the film. Note that in Figures 4.10, 4.11. and 4.12, the black portions at the top of the figure are the carbon bakelite hot press mount used to protect the coating during the polishing process, as well as prevent charge effects in SEM imaging. The brighter metallic in the center of each image is Ni coating, and the dimmer metallic in the bottom of each image is Ti substrate.

The interface of each film is analyzed in order to study the effect of processing time on interface symmetry (i.e. holes bored into substrate, etc.) as well as to study the formation of any intermetallics resulting from the process.

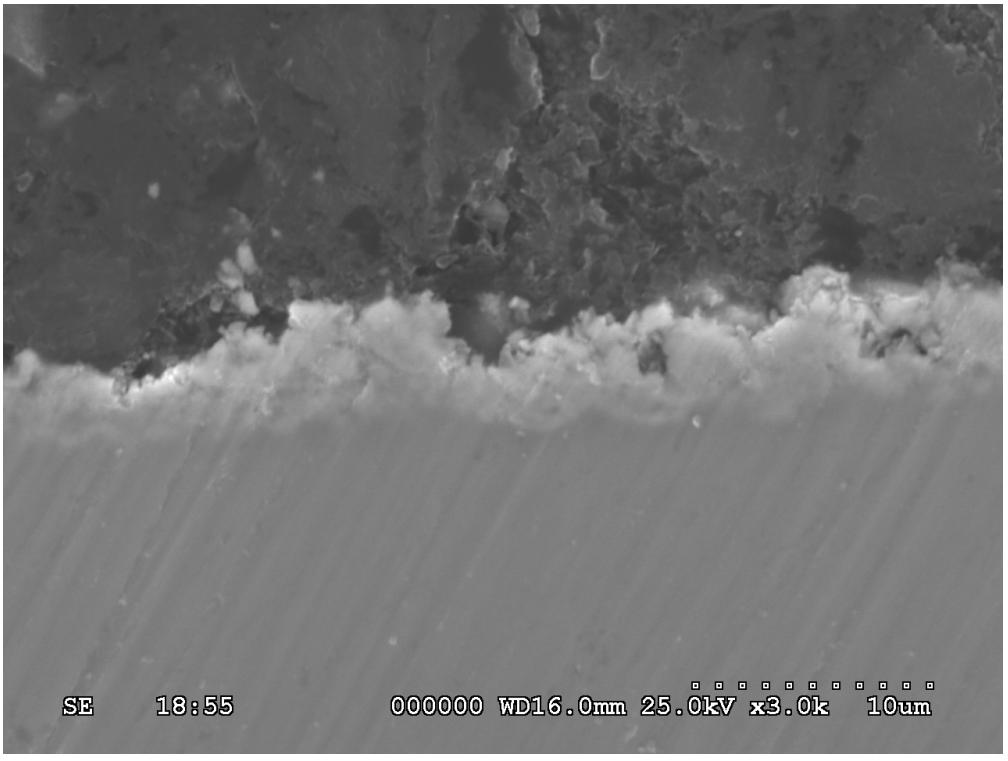

FIGURE 4.10: SEM image of 10s EPP deposited Ni film cross section at 3000x magnification

FIGURE 4.11: SEM image of 20s EPP deposited Ni film cross section at 3000x magnification

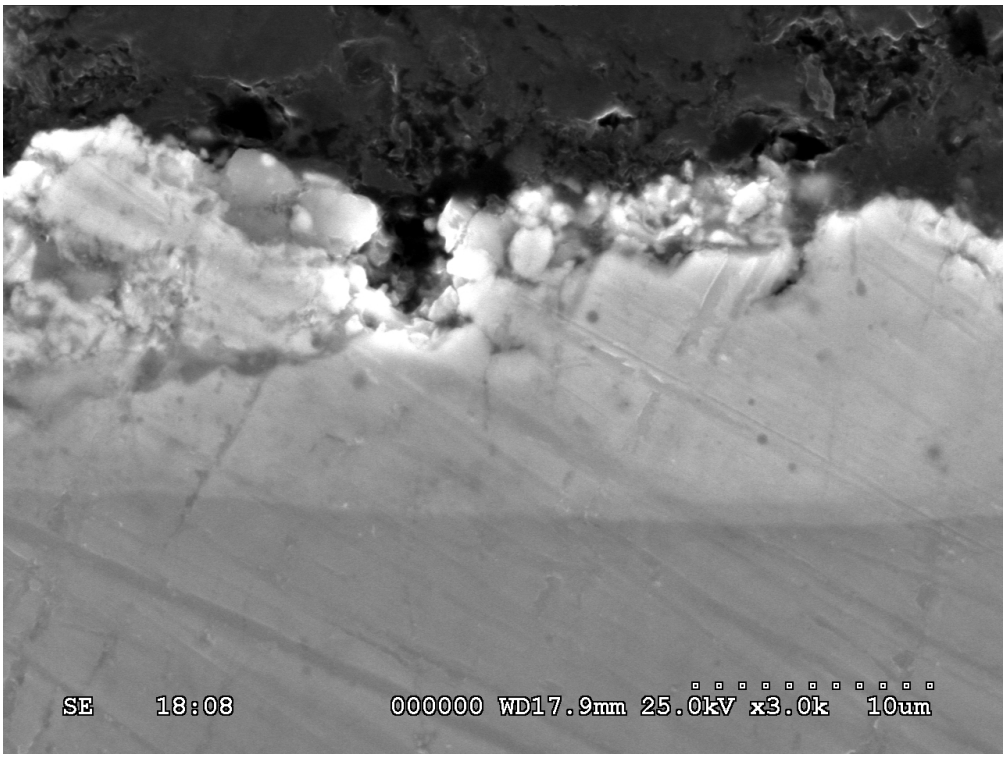

FIGURE 4.12: SEM image of 30s EPP deposited Ni film cross section at 3000x magnification

Utilizing the SEM images displayed in Figures 4.10, 4.11, and 4.12, a growth rate could be calculated. Nine points were selected and measured for thickness in each film. The average thickness of each film was used to calculate the approximate growth rate of 440 $\frac{nm}{s}$. Note that sections that were missing film entirely were disregarded, such that no sections of zero coating thickness were included in the measurement. While this may introduce some systematic error in the growth rate measurement, sections of film are damaged in the cutting, mounting, and polishing process, as well as instability in the plasma as the process goes on. Additionally, by taking the ratio of missing film to adherent film, we find that the growth rate is only marginally lesser, suggesting that if there were 100% adherence the growth rate would likely remain the same.

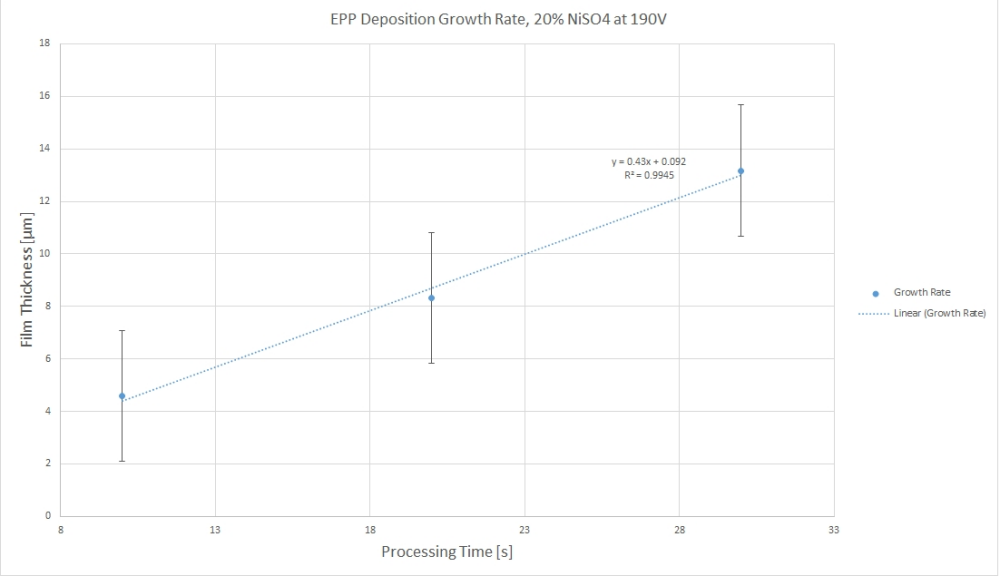

FIGURE 4.13: Calculated growth rate determined by thickness measurements of 9 seperate points in each film

Spot	10 Second	20 Second	30 Second
1	4.3	7.8	13
2	4.6	8.7	13
3	4.2	8.7	13.5
4	3.8	8	13.8
5	5.3	8.3	12.7
6	4.9	7.8	12.6
7	4.5	8.6	13.9
8	4.6	8.3	12.7
9	5	8.7	13.4
Mean	4.578	8.322	13.211
Std Dev.	0.452	0.38	0.489
Std. Error	0.151	0.127	0.161

TABLE 4.3: Thickness measurements and error calculation corresponding to Figure 4.12

Note that measurement spots are selected throughout the entire film surface to ensure that measurement does not occur in tight packets in order to reduce error in calculation. All the samples have identical film surface area (i.e all coating areas are 9.95 mm in diameter), so the nine thickness measurements are approximately spread about an identical length.

4.2.6 Elemental Analysis

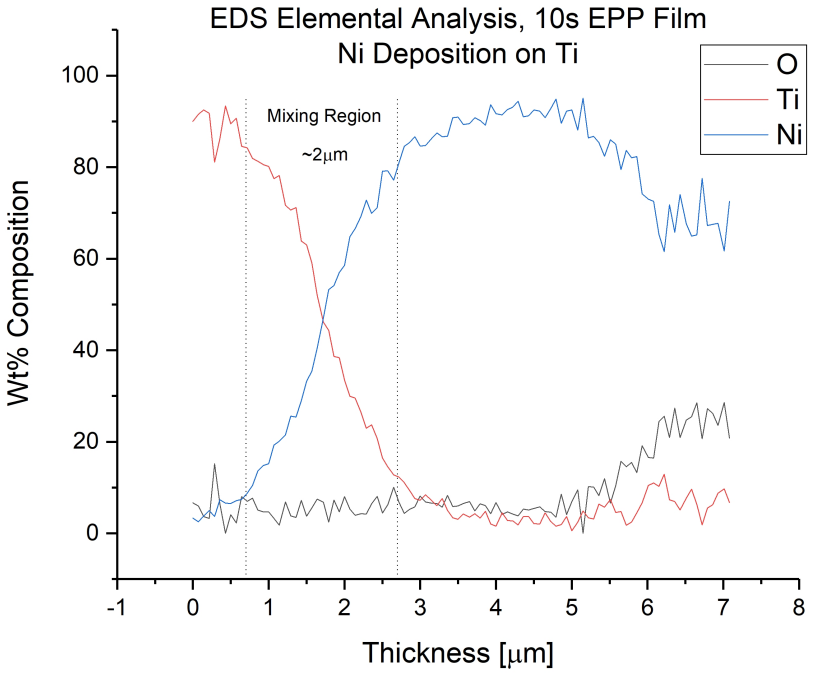

FIGURE 4.14: EDS linescan analysis of elemental wt% in 10 sec. EPP deposition of Ni

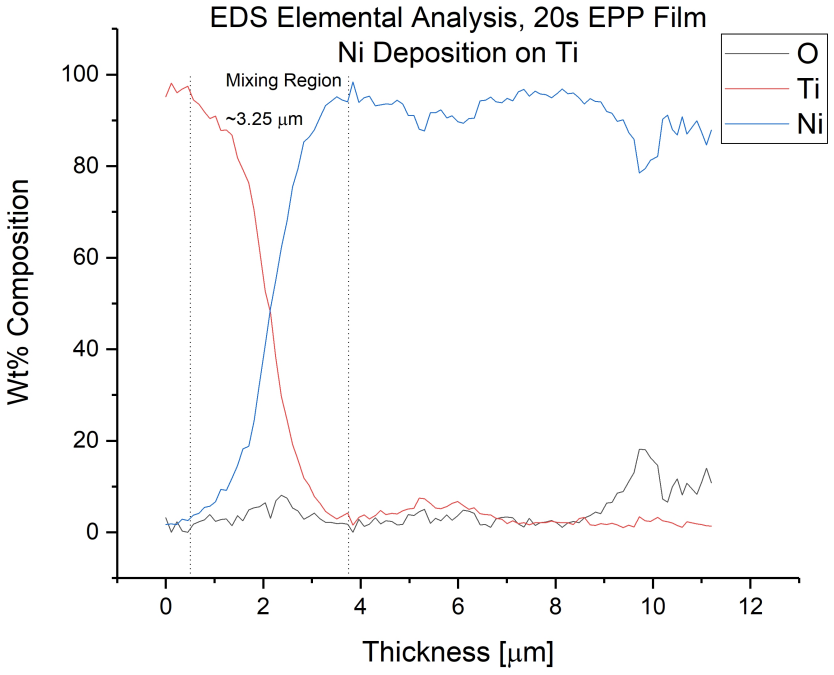

FIGURE 4.15: EDS linescan analysis of elemental wt% in 20 sec. EPP deposition of Ni

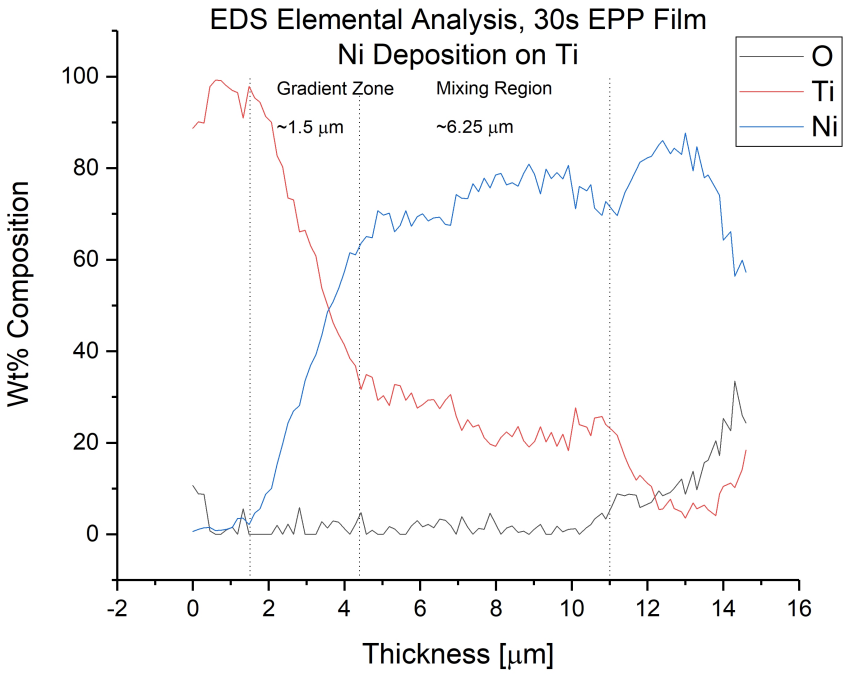

FIGURE 4.16: EDS linescan analysis of elemental wt% in 30 sec. EPP deposition of Ni

The EDS measurements shown in Figures 4.14, 4.15, and 4.16 are measured including a portion of the substrate so as to include the entire interface between film and substrate, as well as a small section (less than one half μm) past the end of the film to determine if an oxide layer exists at the end of the pure Ni top layer. Film thicknesses are still 4.578 μm, 8.322 μm, and 13.211 μm for the 10s, 20s, and 30s depositions respectively.

The wt% shift from predominantly Ti to Ni begins slightly inside of the substrate due to the initial surface melting and forced deposition. For reference, in all three depositions, the Ni content approximately μm inside of the substrate is between 6% and 10%, and the interface occurs between 12% and 15%.

Studying the mixing of Ti and Ni wt% shift throughout the film, we can conclude that there is an initial gradient zone where wt% shifts in and just after the interface, and then Ni dominates the film. Looking to Figures 4.14 and 4.15, the film rapidly becomes

almost purely Ni towards the surface of the coating, while in Figure 4.16, the gradient of mixture extends much deeper into the film. According to these figures, processing with EPP past 20s, we begin to see different intermetallic phases (NiTi, Ni_3Ti, Ti_2Ni, etc.) in the mixing region leading to less dominant Ni wt% until deeper in the film thickness.

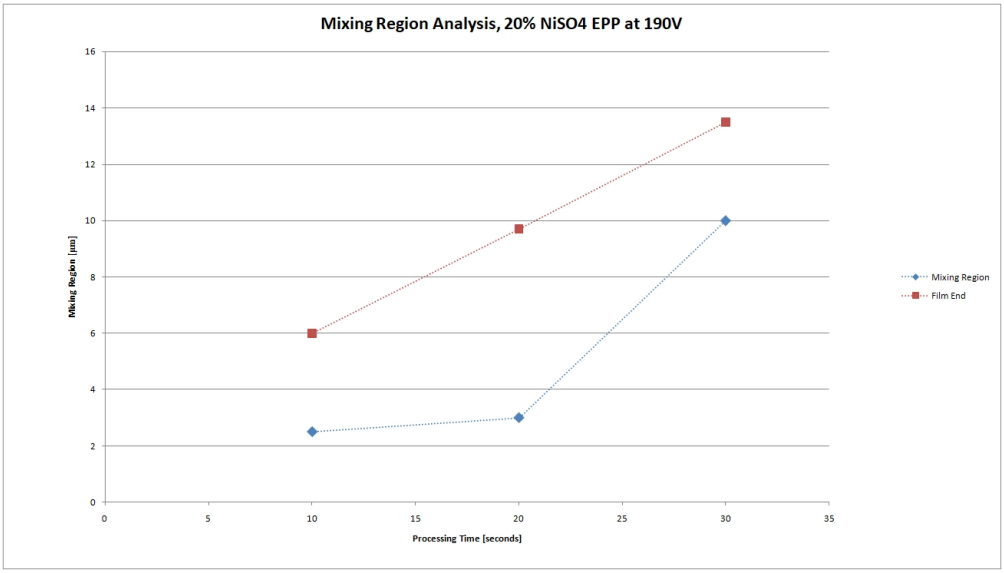

FIGURE 4.17: Analysis of the of Ni-Ti mixing region length vs. start of predomination of Ni in coating thickness

Figure 4.16 compares the length from the interface start to the region where Ni has become completely dominant in the film and the total thickness of the mixing region. This shows the increase in mixing gradient throughout the film when processing for more than 20s, additionally suggesting presence of Ni-Ti intermetallics throughtout the film.

4.2.7 TEM Analysis of the cross section

The following TEM images and analysis were performed in close cooperation with Dr. Jiechao Jiang, coordinator of the UTA Character Center for Materials and Biology and UTA professor. TEM data was deemed necessary in order to confirm or deny the presence of intermetallic compounds beyond a reasonable doubt. The XRD data held

some suggestion of intermetallic compounds, but could not be confirmed via SEM cross section or EDS data.

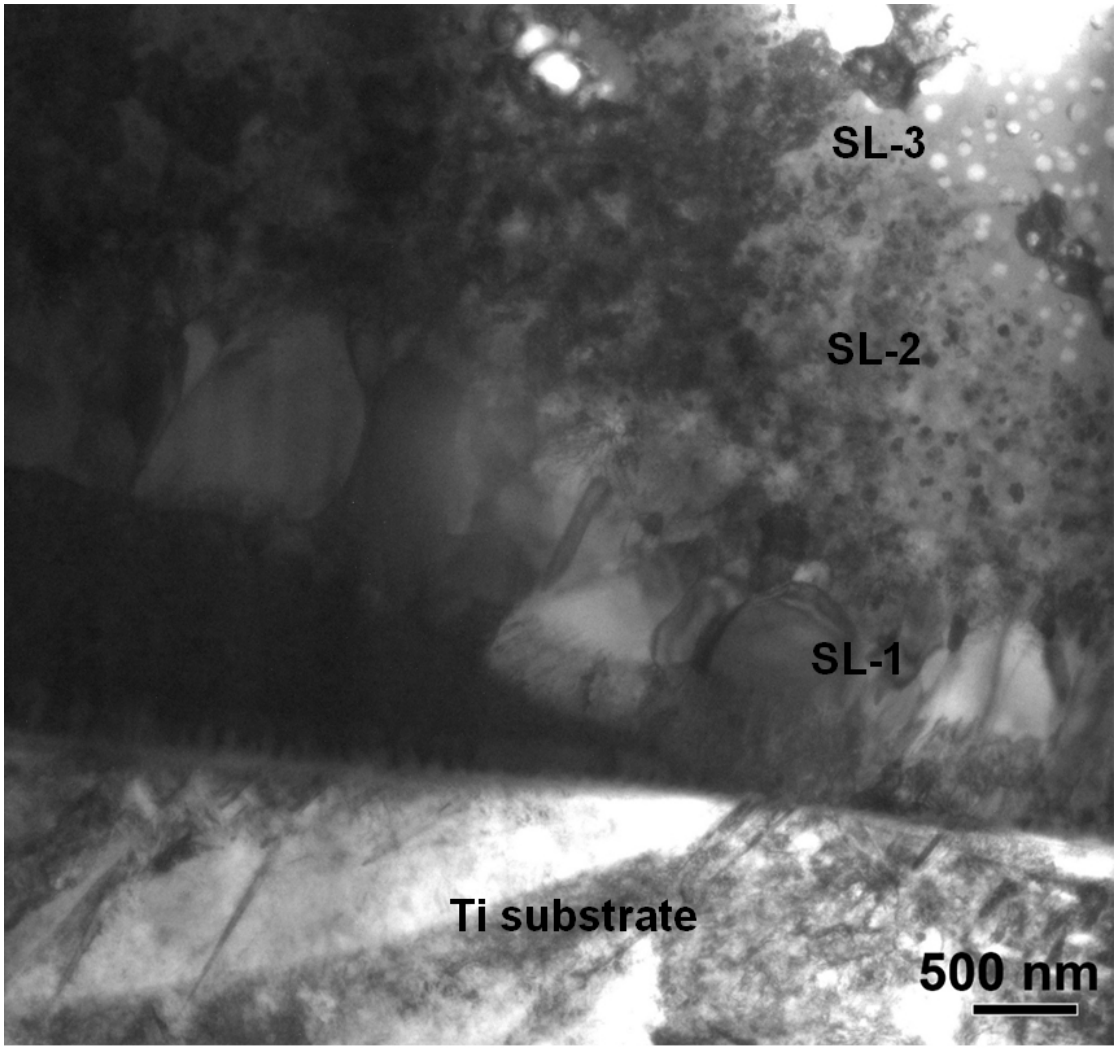

FIGURE 4.18: TEM Image cross section image of the deposited Ni coating on Ti substrate prepared via 30s EPP process

Figure 4.18 is a cross section image taken at the interface to find grain structures matching to known Ni-Ti intermetallics. In Figure 4.18, we find very large grains just past the interface into the Ni coating, with smaller inidicative nanograin structure appearing further into the film. Several sections of the film have been measured via EDS and SAED (selected area electron diffraction) to determine the presence of such compounds.

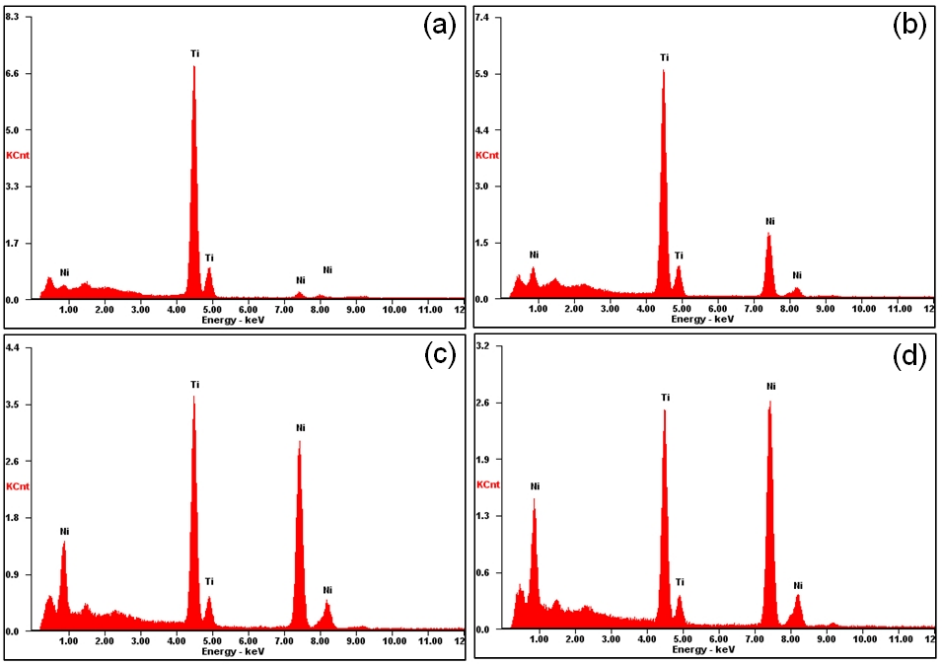

FIGURE 4.19: EDS elemental analysis of TEM sections (a) Ti substrate, (b) SL-1, (c) SL-2, and (d) SL-3 shown in Figure 4.17

TABLE 4.4: EDS wt% corresponding to Figure 4.18

Location	Ti (wt%)	Ni (wt%)
Ti substrate	98	2
SL-1	74	26
SL-2	53	47
SL-3	45	55

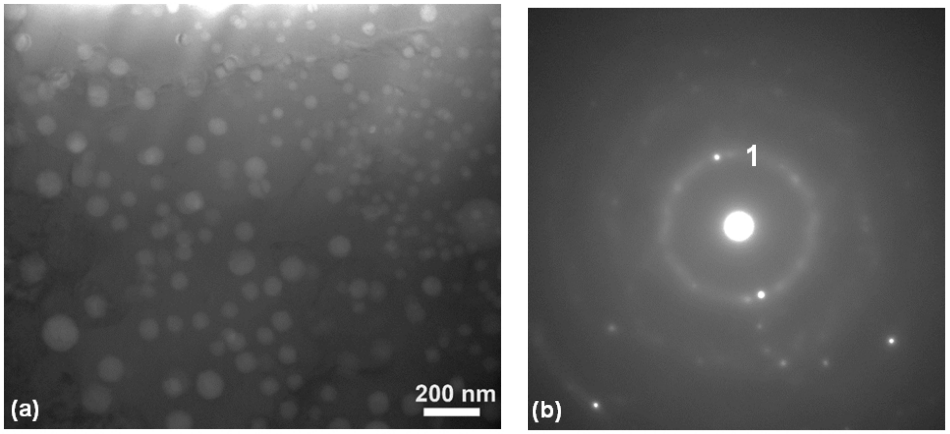

(a) (b)

FIGURE 4.20: Zoom in TEM image of the SL-3 layer shown in Figure 4.17 (a) and SAED of the selected area (b). Image (b) has a lattice spacing of 2.17Å characteristic of the (110) plane of cubic NiTi

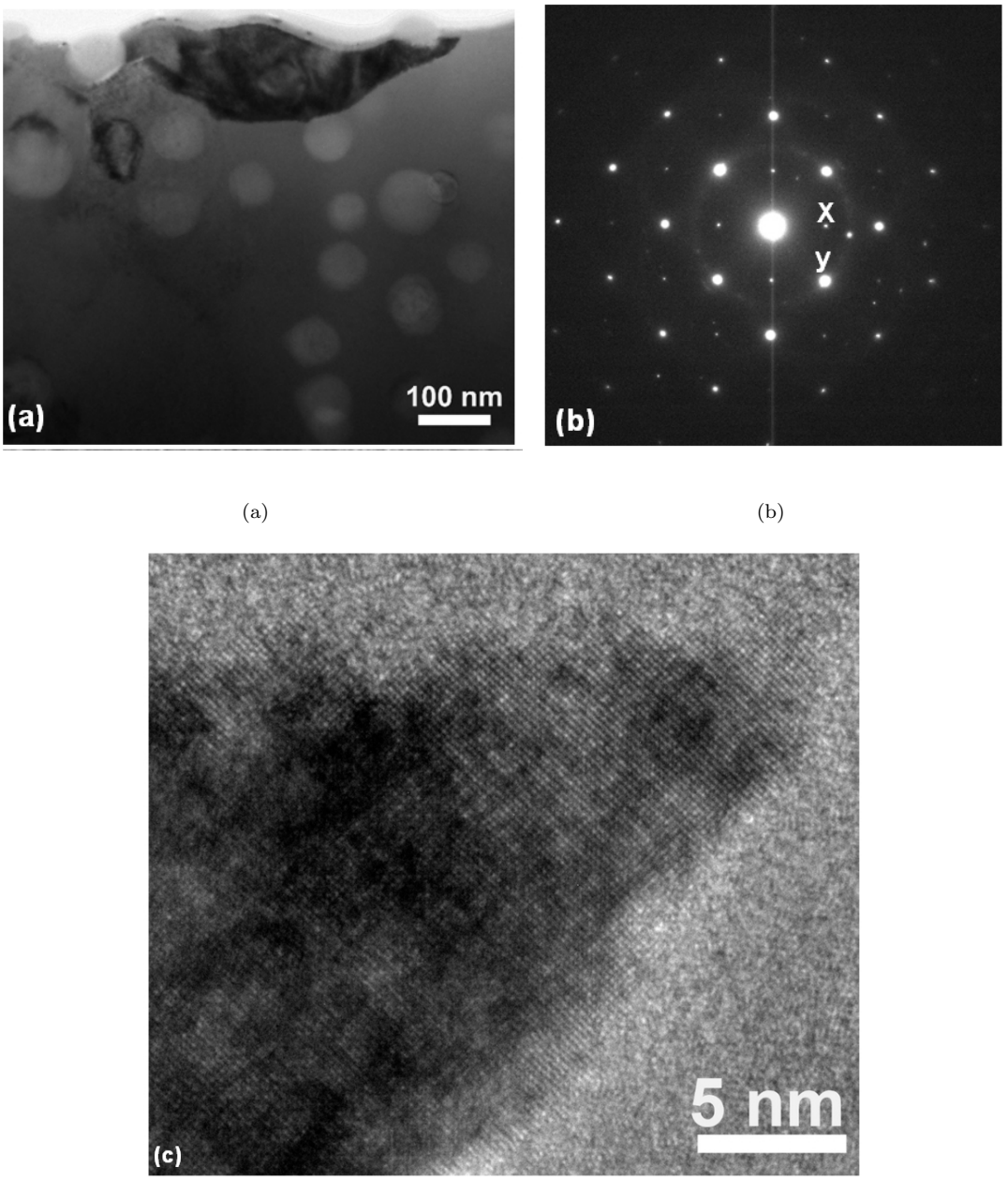

(a) (b)

(c)

FIGURE 4.21: (a) Zoom in TEM image of the SL-3 layer shown in Figure 4.17 presenting a dark grain; (b) SAED pattern from the dark grain showing [0 0 1] zone diffraction pattern of cubic NiTi structure. The diffraction spot x and y has a lattice spacing of 3.01Å and 2.11Å that can be indexed as (1 0 0) and (0 1 1) of NiTi respectively. (c) high-resolution TEM image of the dark grain in image (a).

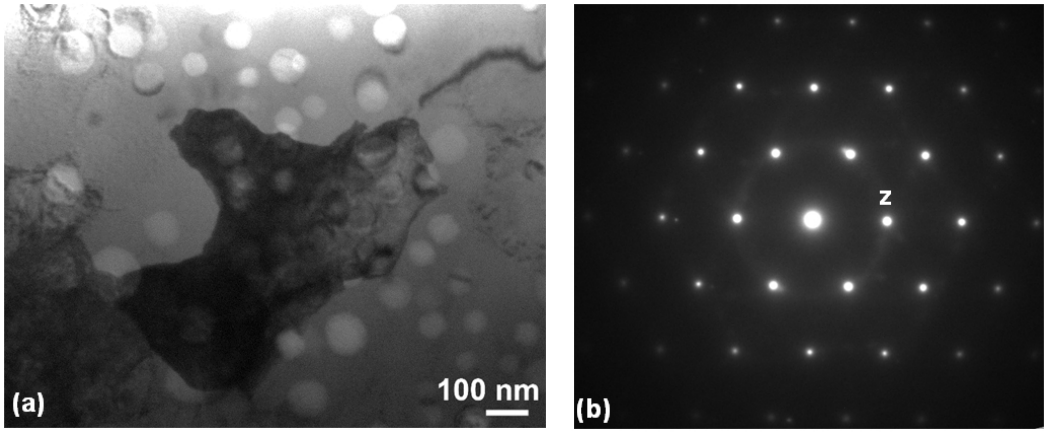

(a) (b)

FIGURE 4.22: (a) Zoomed TEM image of the SL-3 Layer of Ni coating presenting an additional dark grain; (b) SAED pattern of the shown grain showing the [111] plane diffraction pattern of cubic NiTi. Diffraction spot z has a lattice spacing of 2.11Å that can be indexed as (011).

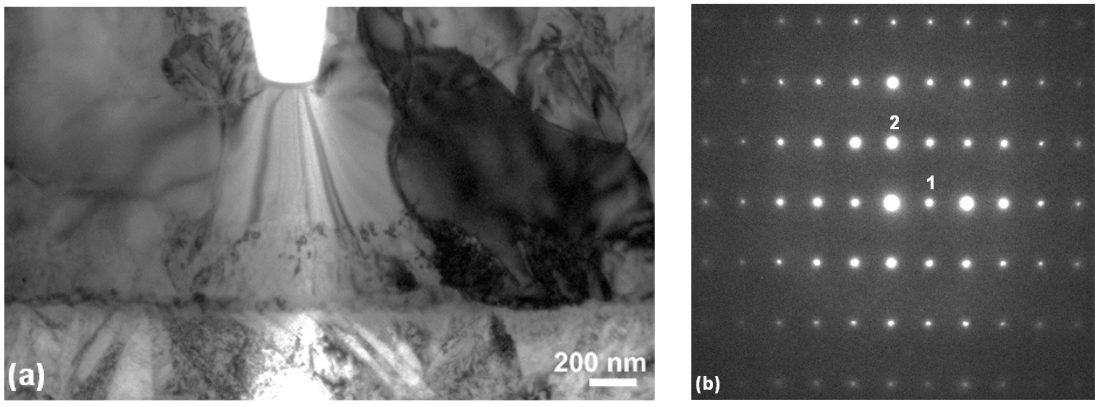

(a) (b)

FIGURE 4.23: (a) Zoomed in TEM image from the Ti substrate and the SL-1 intermetallic layer. The grains in this layer have a size of roguhly 1 μm. (b) SAED pattern taken from the dark grain of image (a) presents a single crystal diffraction pattern. The diffraction spots 1 and 2 in (b) have a lattice space of 6.54Å and 4.06Å respectively. The composition of this grain is approximately Ti_3Ni. This electron diffraction pattern cannot be indexed using any existed available structures indicating a new phase formed in the interlayer. The crystal structure determination of this new structure is in progress.

As stated above, the operation of the TEM, image generation, and analysis was taken on by UTA's Dr. Jiechao Jiang due to restraints in time and a lack of opportunity for training. Dr. Jiang is to be credited with the TEM analysis present in this study.

As the Ti-Ni intermetallic phase detailed in Figure 4.23 cannot be identified via the Ti-Ni phase diagram and matches no existing SAED diffraction pattern, it may be a newly formed non-equillibrium, meta stable intermetallic alloy of the proportions Ti_3Ni.

4.3 Microhardness of the Interface

Since intermetallic compound formation has been definitively shown, it is important to begin characterization of the intermetallic compounds. Specifically, the microhardness of the intermetallic region is important to discern. Cross sectioned, hard-mounted samples were taken to the microindenter to determine a relationship between hardness and distance from the interface. Due to the EDS, XRD, and TEM results, we conclude that majority of intermetallic compounds lie just inside the interface (within a few μm) for 10s and 20s depositions, and may lie a further (within 6-10 μm) for 30s depositions. A 25gf load was chosen so as to ensure visibility of indents, minimize damage to the surface, and increase the amount of measurements that could be done through the thickness of the film. Even using such small load, the 10s film was too small to produce any meaningful hardness results.

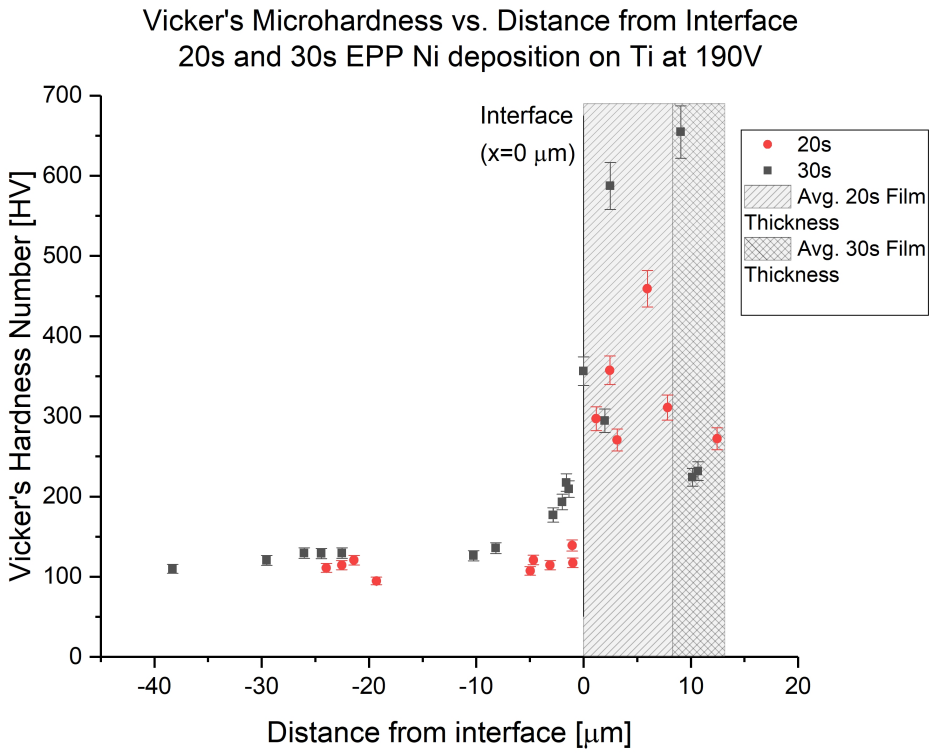

FIGURE 4.24: Measured microhardness vs. distance from interface of 20s and 30s EPP depositions

Ti hardness remains uniform far away from the film, and we see noted increases in hardness once within a few μm of the interface. Hardness of the 20s sample is at it's highest near the interface while the hardness of the 30s sample is at it's highest a few (up to 9) μm further into the film. This lends creedence to mixing effect displayed in Figure 4.16, where we can observe Ti-Ni mixing throughout the entirety of the film, as opposed to Figure 4.15, where the mixing region is quite brief.

(a)

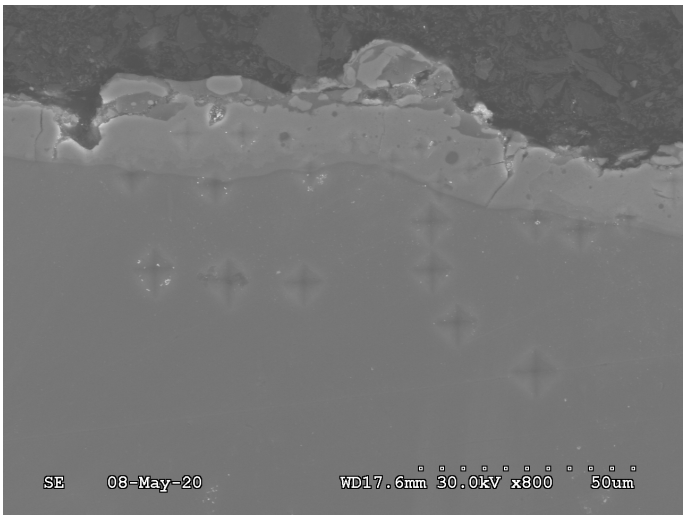

(b)

FIGURE 4.25: SEM micrographs of Vicker's hardness indents at the interface of the 20s and 30s EPP depositions of Ni on Ti

As a comparison to Figure 2.1, the samples have been broken into 4 regions each:

- Ti Substrate
- Interface
- Intermetallic Region
- Ni coating

An average of the points falling within each region is generated and plotted in Figure 4.26:

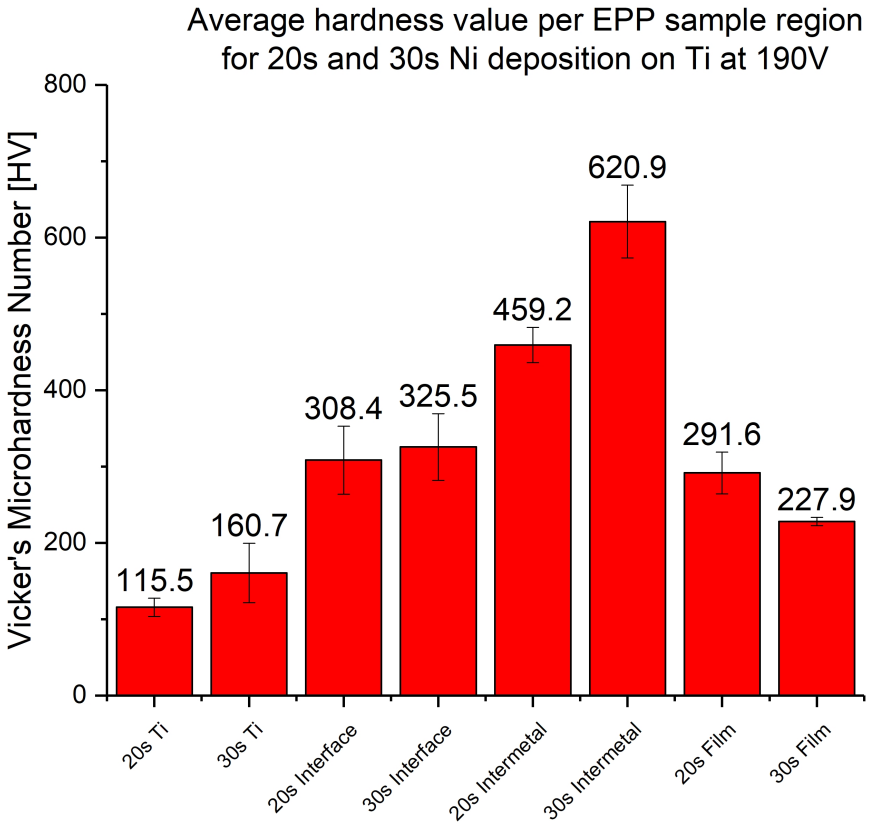

FIGURE 4.26: Average microhardness of the Ti substrate, interface, intermetallic region, and Ni film of 20s and 30s EPP depositions

The hardness at the Ni coating surface is expected to match pure Ni much closer than detailed here, however measurement of this region could not be performed without influence from the bakelite hardmount. Although such measurements could not be obtained, there exists a clear treand of hardness depreciation nearing the film edge, suggesting that the hardness here returns to a close to pure Ni level.

4.4 Corrosion Resistance of EPP Deposited Ni on Ti

Anodic polarization curves were generated in open air in 3.5% NaCl electrolyte at room temperature. A summary of the corrosion potentials and corrosion currents are calculated from experiment for pure Ni, pure Ti, and 10s, 20s, 30s EPP Ni deposited on Ti. The greatest corrosion resistance was found to be the 10s EPP deposited sample, with the 20s and 30s samples acting almost the same through the entire process. All three coated samples were found have better corrosion resistance than the pure metals. All 3 deposited samples were shown to pass through a passivation region and then exhibit activity. The 20s and 30s samples both showed visible degradation from the process, while the 10s samples showed no visible disturbance post-process.

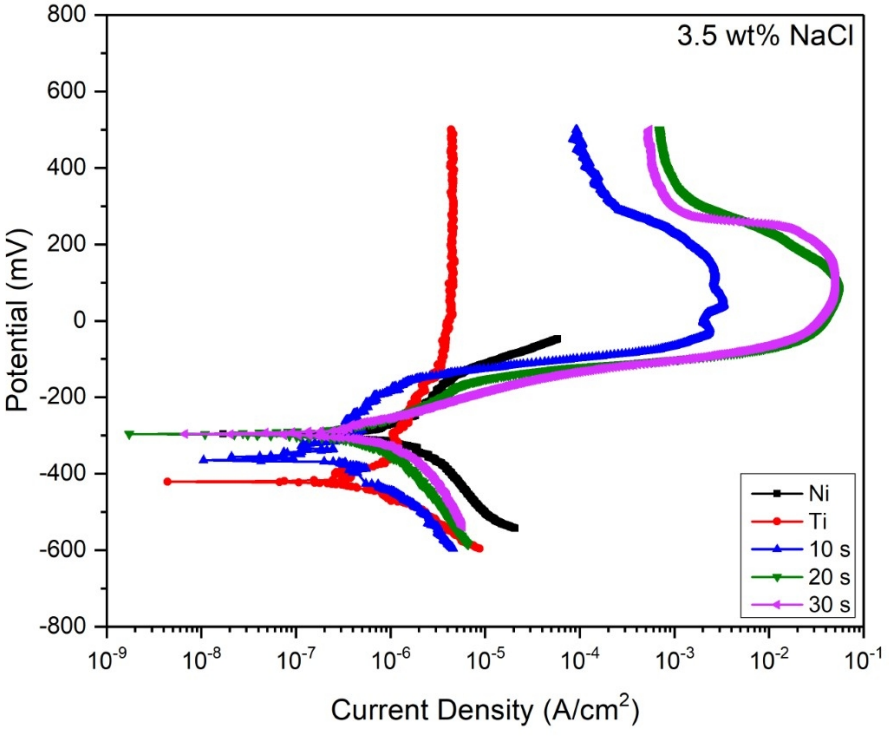

FIGURE 4.27: Anodic polarization of pure Ni, pure Ti, 10s, 20s, and 30s EPP Ni depositions on pure Ti at 190V

TABLE 4.5: Corrosion potentials and corrosion rates for pure Ni, pure Ti, and 10s, 20s, and 30s EPP deposited Ni on Ti

Material	E_c (mV)	I_c (μA / cm_2)	$\beta_c(mV/dec)$	β_a (mV / dec)
Ti	-414.6	0.68	171.2	457.0
Ni	-295.1	1.07	193.4	226.6
10s	-344.4	0.32	196.7	408.4
20s	-294.0	0.42	205.4	118.3
30s	-275.4	0.53	151.6	63.7

Note that these corrosion rates are calculated utilizing the surface area not including roughness within the coatings. Taking into account that the roughness of the 20s and 30s sample could increase the surface area in a non-trivial fashion, the corrosion rates may actually be closer to, or better than the 10s sample. However, if we utilize the surface area of just the surface and do not account for roughness, the coated samples are comparable to each other, and corrode slower than the pure metals.

A reasonable SEM micrograph could not be generated from the 20s or 30s surfaces as the activation caused significant damage to the surface. Althought sections of the film remain, it can be concluded that there is strong activation at sections with less film as we have confirmed that the film is varied in thickness and voracity. Additionally, some additional corrosion rate may exist from microcracks and voids caused by arcing in the initial deposition process, lending to additional activation sites that might not exist otherwise.

4.5 Discussion/Conclusions

The EPP deposition process of Ni onto Ti resulted in a nanograin surface stucture that increases with continuity and roughness as processing time goes on. While nanograins are visible via TEM analysis, an intermetallic layer exists near the interface with larger micrograins. In this intermetallic layer, stoichiometric NiTi grains have been confirmed

along with a new intermetallic compound with approximate wt% equaling that of Ti_3Ni. The discovery of this new intermetallic compound requires additional study for further confirmation and analysis, but it adequatley shows that the EPP process can reliably create layers of intermetallics like the shape memory alloy NiTi. Hardness of the resultant intermetallic layer is studied and found to be significantly harder than the Ti substrate or pure Ni alone. Hardness values in the intermetallic region peak at 700 HV, matching accepted hardness values for Ti-Ni intermetallics like Ti_2Ni. EPP deposited Ni films on pure Ti have been shown to have improved corrosion properties over Ti or Ni alone. All three depositions of films exhibit passivation and lower corrosion rates than the pure metals, with the 10s sample delivering the best results, and the 20s and 30s samples showing comparable rates to the 10s samples when utilizing a non-rough surface calculation. Furthermore, the EPP process has been confirmed to retain the expected linear growth relationship due to collapse and pressurization of plasma bubbles, rather than a non-linear diffusion process while forming intermetallic alloys at the interface. The formation of intermetallics via EPP has been lightly studied, but these results show promise for the creation of other intermetallics (Ni-Al alloys, etc.) within layers of nanograin surface coating.

Bibliography

H.C. Man, K.L. Ho, and Z.D. Cui. Laser surface alloying of niti shape memory alloy with mo for hardness improvement and reduction of ni2+ ion release. *Surface and Coatings Technology*, 2006.

N.C. Reddy, B.S.A Kumar, H.N. Reddappa, M.R. Ramesh, K.G. Koppad, and S. Kord. Hvof sprayed ni3ti and ni3ti+(cr3c2+20nicr) coatings: Microstructure, microhardness and oxidation behaviour. *Journal of Alloys and Compounds*, 2018.

F. Gao and H.M. Wang. Dry sliding wear property of a laser melting/deposited ti2ni/tini intermetallic alloy. *Intermetallics*, 2008.

D. Batalu, H. Guoqiu, A. Aloman, G. Cosmeleata, L. Xiaoshan, and Z. Zhihua. A review on tini shape memory alloys (sma) used for medical applications. recycling aspects. *Research Gate*, 2020.

P. Gupta, G. Tenhundfeld, E.O. Daigle, and D. Ryabkov. Electrolytic plasma technology: Science and engingeering -an overview. *Surface and Coatings Engineering*, 201, 2007.

P.D. Miller and J.W. Holladay. Friction and wear properties of titanium. *Wear*, 2 (2):133–140, November 1958. URL www.sciencedirect.com/science/article/abs/pii/0043164858904289.

A.L Rominiyi, M.B. Shongwe, E.N. Ogunmuyiwa, B.J. Babalola, P.F. Lepele, and P.A. Olubambi. Effect of nickel addition on densification, microstructure and wear behaviour of spark plasma sintered cp-titanium. *Materials Chemistry and Physics*, 240 (122130), January 2020.

T.M. Muraleedharan and E.I. Meletis. Surface modification of pure titanium and ti6-a1-4v by intensified plasma ion nitriding. *Thin Solid Films*, 1992.

D. Starosvetsky and I. Gotman. Corrosion behavior of titanium nitride coated ni–ti shape memory surgical alloy. *Biomaterials*, 2001.

Cristian Cionea. *Microstructural Evolution of Surface Layers During Electrolytic Plasma Processing*. PhD thesis, University of Texas at Arlington, 2010.

Adam Smith. *Surface Modification of Iron and Aluminum by Electrolytic Plasma Processing*. PhD thesis, University of Texas at Arlington, 2014.

Nastaran Barati. *An Investigation of the plasma electrolytic oxidation mechanism for coating of alumina-zirconia nanocomposite*. PhD thesis, University of Texas at Arlington, 2018.

X. Song, J. Lei, J. Xie, and Y. Fang. Microstructure and electrochemical corrosion properties of nickel-plated carbon nanotubes composite inconel718 alloy coatings by laser melting depositon. *Optics and Laser Technology*, 119, November 2019.

H-R. Stock, M. Diesselberg, and Zoch H.W. Investigation of magnetron sputtered titanium-nickel-nitride thin fiulms for use as mould coatings. *Surface and Coatings Technology*, 203:717–720, December 2008.

M. Chandrakala, S.R. Bharath, T. Maiyalagan, and S. Arockiasamy. Synthesis, crystal structure and vapour pressure studies of novel nickel complex as precursor for nio

coating by metalorganic chemical vapour deposition technique. *Materials Chemistry and Physics*, 201:344–353, November 2017.

M-J. Liu, M. Zhang, X-F. Zhang, G-R. Li, Q. Zhang, C-X. Li, C-J. Li, and G-J. Yang. Transport and deposition behaviors of vapor coating materials in plasma spray-physics vapor deposition. *Applied Surface Science*, 486:80–92, August 2019.

S. Wei, X. Zhan, Y. Wein, Y. Li, Z. Zhang, F. Wu, and C Wang. Deposition mechanism of electroless nickel plating of composite coatings on magnesium alloy], volume = 207, year = 2019. *Chemical Engineering Science*, pages 1299–1308, November .

P. Sahoo and S.K. Das. Tribology of electroless nickel coatings - a review. *Materials and Design*, 32, April 2011.

D. Umapathi, A. Devaraju, C. Rathinasuriyan, and A. Raji. Mechanical and tribological properties of electroless nickel phosphorous and nickel phosphorous-titanium nitride coating. *Materialstoday: Proceedings*, 22, 2020.

W. Shang, X. Zhan, Y. Wen, Y. Li, Z. Zhang, F. Wu, and C. Wang. Deposition mechanism of electroless nickel plating of composite coatings on magnesium alloy. *Chemical Engineering Science*, 207, 2019.

Y.R. Wang, K. Zheng, R.Y. Wang, Y.S. Wang, J. Gao, Y.F. Liang, Y. Ma, B. Zhou, S.W. Yu, B. Tang, Y.L. Wang, J.P. Lin, and Y.C. Wu. Synthesis, structure, and properties of the high nb–tial alloy after ni coatings by plasma surface alloying technique. *Vacuum*, 172, February 2020.

D.J. Guidry, K. Lian, J.C. Jiang, and E.I. Meletis. Tribological behavior of nanocrystalline nickel. *Journal of Nanoscience and Nanotechnology*, 9, 2009.

R.R Adharapurapu. Phase transformations in nickel-rich nickel-titanium alloys: influence of strain-rate, temperature, thermomechanical treatmetn and nickel composition on the shape memory and superelastic characteristics. *eScholarship*, 2007.

C.J. Huang, X.C. Yan, W.Y. Li, W.B. Wang, C. Verdy, M.P. Planche, H.L. Liao, and G. Montavon. Post-spray modification of cold-sprayed ni-ti coatings by high-temperature vacuum annealing and friction stir processing. *Applied Surface Science*, 451, 2018.

A. Fattah-alhosseini, K. Babaei, and M. Molaei. Plasma electrolytic oxidation (peo) treatment of zinc and its alloys: A review. *Surfaces and Interfaces*, 18, 2020.

E. Nikoomanzari, A. Fattah-alhosseini, M.R.P. Alamoti, and M.K. Keshavarz. Effect of zro2 nanoparticles addition to peo coatings on ti–6al–4v substrate: Microstructural analysis, corrosion behavior and antibacterial effect of coatings in hank's physiological solution. *Ceramics International*, 2020.

Golsa Mortazavi. *INVESTIGATION OF THE PLASMA ELECTROLYTIC OXIDATION MECHANISM OF TITANIUM*. PhD thesis, University of Texas at Arlington, 2017.

E.I. Meletis, X. Nie, F.L. Wang, and J.C. Jiang. Electrolytic plasma processing for cleaning and metal-coating of steel surfaces. *Surface and Coatings Technology*, 2002.

M. Aliofkhazraei and A.S. Roohaghdam. "a novel method for preparing aluminum diffusion coating by nanocrystalline plasma electrolysis. *Electrochemistry Communications*, 2007.

T. Paulmier, J.M. Bell, and P.M. Fredericks. Development of a novel cathodic plasma/electrolytic deposition techniquepart 2: Physico-chemical analysis of the plasma discharge. *Surface and Coatings Technology*, 2007.

A.I. Yerokhin, L.O. Snizhko, N.L. Gurevina, A. Leyland, A. Pilkington, and A. Matthews.